

# Spectral Comparison of Weak Short Bursts to the Persistent X-rays from the Magnetar 1E 1547.0–5408 in its 2009 Outburst

T. Enoto<sup>1,2\*</sup>, Y. E. Nakagawa<sup>3</sup>, T. Sakamoto<sup>2</sup>, and K. Makishima<sup>1,4</sup>

<sup>1</sup> High Energy Astrophysics Laboratory, Institute of Physical and Chemical Research (RIKEN), Wako, Saitama, 351-0198, Japan

<sup>2</sup> Goddard Space Flight Center, NASA, Greenbelt, Maryland, 20771, USA

<sup>3</sup> Research Institute for Science and Engineering, Waseda University, 17 Kikui-cho, Shinjuku-ku, Tokyo 162-0044, Japan

<sup>4</sup> Department of Physics, University of Tokyo, 7-3-1 Hongo, Bunkyo-ku, Tokyo, 113-0033, Japan

12 September 2010

## ABSTRACT

In January 2009, the 2.1-sec anomalous X-ray pulsar 1E 1547.0–5408 evoked intense burst activity. A follow-up *Suzaku* observation on January 28 recorded enhanced persistent emission both in soft and hard X-rays (Enoto et al. 2010b). Through re-analysis of the same *Suzaku* data, 18 short bursts were identified in the X-ray events recorded by the Hard X-ray Detector (HXD) and the X-ray Imaging Spectrometer (XIS). Their spectral peaks appear in the HXD-PIN band, and their 10–70 keV X-ray fluences range from  $\sim 2 \times 10^{-9}$  erg cm<sup>-2</sup> to  $10^{-7}$  erg cm<sup>-2</sup>. Thus, the 18 events define a significantly weaker burst sample than was ever obtained,  $\sim 10^{-8}$ – $10^{-4}$  erg cm<sup>-2</sup>. In the  $\sim 0.8$  to  $\sim 300$  keV band, the spectra of the three brightest bursts can be represented successfully by a two-blackbody model, or a few alternative ones. A spectrum constructed by stacking 13 weaker short bursts with fluences in the range  $(0.2\text{--}2) \times 10^{-8}$  erg s<sup>-1</sup> is less curved, and its ratio to the persistent emission spectrum becomes constant at  $\sim 170$  above  $\sim 8$  keV. As a result, the two-blackbody model was able to reproduce the stacked weaker-burst spectrum only after adding a power-law model, of which the photon index is fixed at 1.54 as measured in the persistent spectrum. These results imply a possibility that the spectrum composition employing an optically-thick component and a hard power-law component can describe wide-band spectra of both the persistent and weak-burst emissions, despite a difference of their fluxes by two orders of magnitude. Based on the spectral similarity, a possible connection between the unresolved short bursts and the persistent emission is discussed.

**Key words:** stars: pulsars: general – pulsars: individual (1E 1547.0–5408, SGR J1550–5418, PSR J1550–5418, G327.24–013)

## 1 INTRODUCTION

Magnetars are a peculiar subclass of isolated neutron stars (Duncan & Thompson 1992; Thompson & Duncan 1995) with evidence for ultra-strong magnetic fields, mainly emitting in the X-ray frequency. Located along the Galactic plane and in the Magellanic Clouds,  $\sim 9$  soft gamma repeaters (SGRs) and  $\sim 12$  anomalous X-ray pulsars (AXPs) are currently believed to be of the magnetar class (for reviews, see Woods & Thompson 2006; Mereghetti 2008). X-ray pulsations have been observed from them in a period range of  $P = 2\text{--}12$  s, indicating slowly rotating iso-

lated pulsars. Together with their large period derivatives  $\dot{P} \sim 10^{-12} - 10^{-10}$  s s<sup>-1</sup>, the magnetic-dipole-radiation approximation indicates these objects to have ultra-strong magnetic fields of  $B = 3.2 \times 10^{19} \sqrt{P\dot{P}}$  G  $\gtrsim 3.3 \times 10^{13}$  G. Thus, it is widely believed that the peculiar characteristics of SGRs and AXPs originate from their extremely strong magnetic fields.

The X-ray radiation from magnetars emerges on a large variety of time scales and intensities. One form is “persistent” X-ray emission with a typical luminosity of  $L_x \sim 10^{35}$  erg s<sup>-1</sup>, which is usually stable over long periods of time ( $\sim$  a few month or longer). A typical persistent X-ray luminosity of magnetars exceeds by 1–2 orders of magnitude that available from their rotational energy losses,  $\sim 10^{33\text{--}34}$

\* E-mail: enoto@stanford.edu

erg  $s^{-1}$ . Without evidence for mass accretion, the emission is therefore considered to be powered by dissipation of the magnetic energies. The broad-band persistent X-ray spectrum is generally composed of blackbody-like soft X-ray component with a temperature of  $\sim 0.3\text{--}0.5$  keV (Mereghetti 2008; Rea et al. 2007; Enoto et al. 2011), and a power-law-like hard X-ray component with a photon index of  $\Gamma \sim 1$  (Kuiper et al. 2006; den Hartog et al. 2008; Enoto et al. 2010c). While the soft component can be considered as optically-thick thermal radiation from the stellar surface, the hard component, spanning from  $\sim 10$  keV to  $\sim 200$  keV or higher, is considered to emerge through a different and yet unidentified process (e.g., Thompson & Beloborodov 2005; Beloborodov & Thompson 2007; Baring & Harding 2007; Fernández & Thompson 2007; Heyl & Hernquist 2005).

Another form of X-ray radiation from magnetars is sporadic emission of bursts with a typical duration from  $\sim 0.1$  seconds to a few hundred seconds. These bursts are phenomenologically classified into three types: quite rare “giant flares” with  $L_x \gtrsim 10^{45}$  erg  $s^{-1}$  lasting about a few hundred seconds (Mazets et al. 1979; Feroci et al. 2001; Hurley et al. 2005), “intermediate flares” with  $L_x \sim 10^{42} - 10^{43}$  erg  $s^{-1}$  lasting a few seconds (Kouveliotou et al. 2001; Olive et al. 2004; Israel et al. 2008), and much more frequently occurring “short bursts” with  $L_x \sim 10^{38} - 10^{41}$  erg  $s^{-1}$  with  $\sim 0.1$ -sec durations (Nakagawa et al. 2007b; Israel et al. 2008). Thus, these explosive events often show luminosities exceeding the Eddington limit for a neutron star of  $1.4M_\odot$  ( $M_\odot$  being the solar mass),  $L_{\text{Edd}} \sim 1.8 \times 10^{38}$  erg  $s^{-1}$ , presumably due to suppression of the electron scattering cross sections in the strong field (Paczynski 1992). The mechanisms of these bursts are thought to be related to rearrangement of the magnetic fields invoking reconnection (Lyutikov 2003), or motion and fracturing of the neutron star crust, i.e., starquake (Thompson et al. 2002).

The persistent X-ray intensity of a magnetar sometimes increases by 1–2 orders of magnitude with unpredictable timing. Such an transient enhancement lasts typically for a few months, including its gradual decay. They are often accompanied, at its early phase, by a burst activity, which can even lead to discoveries of new magnetars. So far, such burst-active states, or outbursts, were observed from some magnetars; XTE J1810–197 (Gotthelf et al. 2004; Ibrahim et al. 2004; Israel et al. 2004; Gotthelf & Halpern 2005; Bernardini et al. 2009), CXOU J164710.2–455216 (Muno et al. 2007; Israel et al. 2007), SGR 0501+4516 (Enoto et al. 2009; Rea et al. 2009; Enoto et al. 2010a), and 1E 1547.0–5408 (Mereghetti et al. 2009; Enoto et al. 2010b). More recently, there have been accumulating reports on such activities from sources with much weaker dipole fields ( $\lesssim 4.4 \times 10^{13}$  G); SGR 0418+5729 (van der Horst et al. 2010; Rea et al. 2010), SGR 1833–0832 (Gögüş et al. 2010; Esposito et al. 2011), Swift J1822.3–1606 (Rea et al. 2012), and Swift J1834.9–0846 (Kargaltsev et al. 2012).

The enhanced persistent emission and the burst activity have been simultaneously observed in many activated magnetars. However, it is not yet clear how these two emission forms are physically related with each other in the postulated dissipation process of the magnetic energy. One interesting possibility is that the persistent emission is composed of a large number of small bursts that are not individually detectable (e.g., Thompson & Duncan 1996; Lyutikov

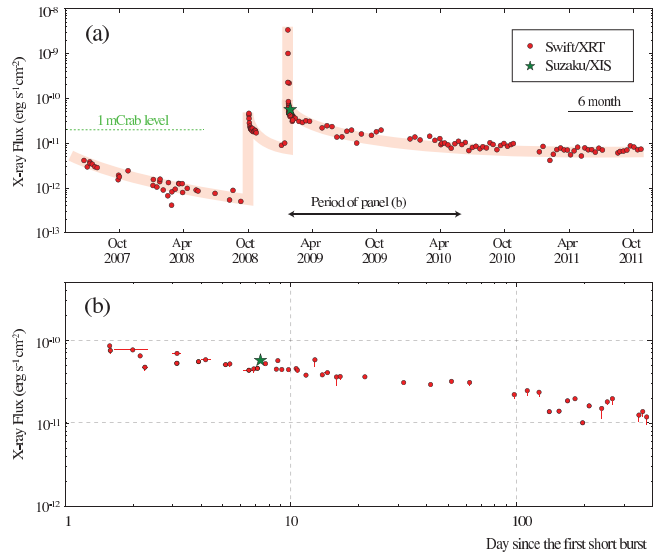


**Figure 1.** Long-term X-ray monitoring of 1E 1547.0–5408 with the *Swift*/XRT, produced from the public *Swift* data archive through a standard analyses procedure, fitted by an absorbed blackbody spectrum with the absorption left free. (a) The absorbed 2–10 keV X-ray flux is shown since 2007 May. The *Suzaku* observation is shown in the star (green). (b) An expanded view of panel (a) during the 2009 outburst. The decay is shown as a double logarithmic plot since the first short burst (2009-01-22 01:32:41; Gronwall et al. 2009).

2003; Nakagawa 2007a). Such a possibility has been examined using a cumulative number-intensity distribution of short bursts (Götz et al. 2006; Nakagawa et al. 2007b). However, the observational information has so far remained insufficient to evaluate this possibility, since the studied short bursts are so bright (with fluence  $\gtrsim 10^{-7}$  ergs  $cm^{-2}$ ) and infrequent that their time-averaged flux is much lower than that of the persistent emission. Therefore, it is interesting to examine, from observations of activated magnetars, whether weaker short bursts become similar in spectral shape to the persistent X-ray emission, as recently found in SGR 0501+4516 (Nakagawa et al. 2011).

In the present paper, we studied the activated magnetar 1E 1547.0–5408. Following its discovery by the *Einstein Observatory* (Lamb & Markert 1981) in 1980 and confirmation by *ASCA* (Sugizaki et al. 2001), this object was recognized as a magnetar candidate, located at the center of the supernova remnant G327.24–013 (Gelfand & Gaensler 2007), based on its X-ray spectrum from *XMM-Newton* and *Chandra* observations. This was followed by a discovery of its radio pulsations at  $\sim 2.07$  s (PSR J1550–5418; Camilo et al. 2007), and of X-ray pulsations at the same period (Halpern et al. 2008). Together with a measured period derivative,  $\dot{P} \sim 2.3 \times 10^{-11}$  s  $s^{-1}$  (Camilo et al. 2007), its characteristic age and surface magnetic field intensity were estimated to be 1.4 kyr and  $2.2 \times 10^{14}$  G, respectively; both parameters fall in the magnetar regime. At present, 1E 1547.0–5408 is one of the fastest rotating objects among the known magnetars.

Figure 1 shows a long-term monitoring of the 2–10 keV persistent emission from 1E 1547.0–5408. In 2007, a small enhancement was observed in its persis-

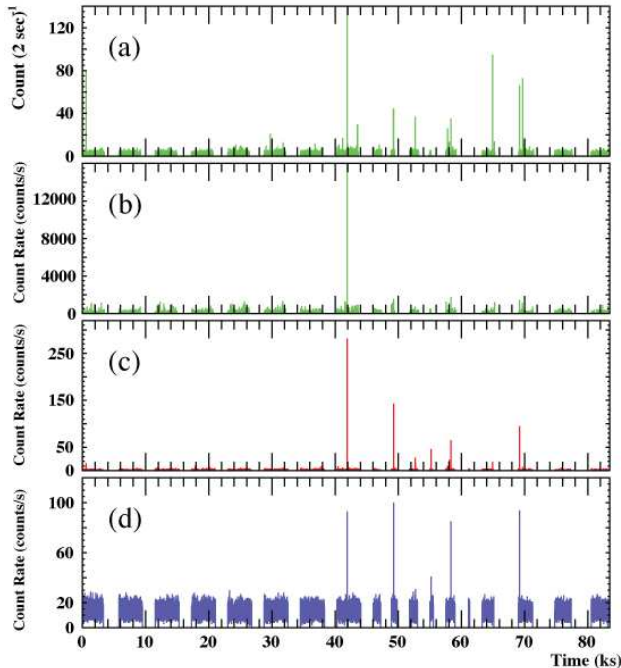


**Figure 2.** Background-inclusive count rates of 1E 1547.0–5408 during the present *Suzaku* observation performed on 2009 January 28. From top to bottom, panels refer to those obtained with XIS1 plus XIS3 (2–10 keV), XIS0 (2–10 keV), HXD-PIN (10–70 keV), and HXD-GSO (50–150 keV). Data are binned into 1 sec, except for 2 sec of panel (a).

tent luminosity (Halpern et al. 2008). In 2008 October, short bursts and decaying persistent soft X-rays have been monitored by *Swift* (Israel et al. 2010). Three month later, a much stronger burst activity, to be dealt with in the present paper, was detected on 2009 January 22 (UT). A series of intense short bursts were recorded by several satellites; *Swift* (Gronwall et al. 2009), *INTEGRAL* (Savchenko et al. 2009), *Suzaku* (Terada et al. 2009), the *Fermi*/GBM (Connaughton & Briggs 2009; von Kienlin & Connaughton 2009), *RHESSI* (Bellm et al. 2009), and *Konus-Wind* (Golenetskii et al. 2009). Some bursts were very bright with fluences above  $\sim 10^{-5}$  erg  $\text{cm}^{-2}$  (Mereghetti et al. 2009), and a 150-s-long enhanced quasi-persistent emission was also recorded on one occasion by the *Fermi*/GBM (Kaneko et al. 2010). Based on these SGR-like activities, 1E 1547.0–5408 was also named SGR J1550–5418 (Kouveliotou et al. 2009).

As shown in Figure 1, the early burst activity was accompanied by a clear enhancement of the persistent emission, which decayed on a timescale of a few month. In Enoto et al. (2010b; hereafter Paper I), we studied persistent emission of this object using the *Suzaku* data acquired on 2009 January 28–29, or  $\sim 7$  days after the burst onset (Figure 1), when the 2–10 keV persistent flux became by 1–2 orders of magnitude higher than that during less active states in 2006 and 2007. On that occasion, a persistent *hard* X-ray component was detected for the first time from this source at least up to  $\sim 110$  keV. The acquired broadband spectrum in 0.7–114 keV was reproduced by an absorbed blackbody (BB) emission with a temperature of  $0.65 \pm 0.02$  keV,

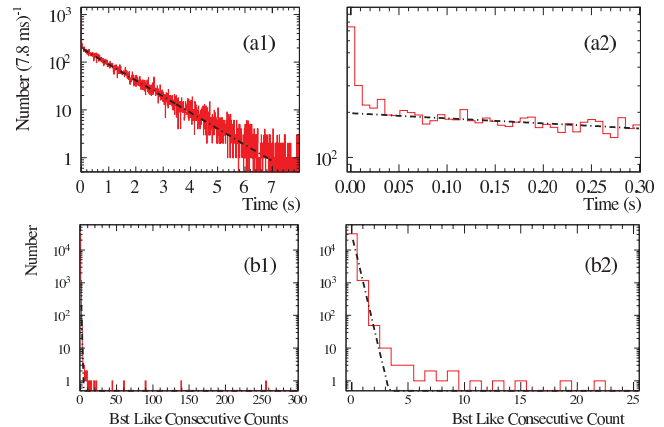


**Figure 3.** (a1) A  $\Delta t$  distribution of the 10–70 keV HXD-PIN events. Dashed-dotted line indicates the best fit exponential model with the average event rate of  $\lambda = 0.778 \pm 0.001$  count  $\text{s}^{-1}$ . (a2) An expanded view of panel (a1) in the 0–0.3 sec range. (b1) Distribution of the consecutive burst-like counts calculated using panel (a). (b2) An expanded view of panel (b1). Dashed-dotted line represents the predicted chance coincidence probability of ordinary events,  $(0.036)^{N_{\text{bst}}}$ .

plus a prominent hard power-law (PL) with a photon index of  $\Gamma_{\text{per}} \sim 1.5$ . The enhanced persistent emission was also studied by *Chandra*, *XMM-Newton*, *Swift*, and *INTEGRAL* (Bernardini et al. 2011; Ng et al. 2011; Kuiper et al. 2009; den Hartog et al. 2009; Bernardini et al. 2011).

In this paper, we present spectral studies of short bursts detected with *Suzaku* in the 2009 observation. The low background of *Suzaku*, especially in the hard X-ray band, allowed us to detect much weaker short bursts than observed so far from any magnetars. Unless otherwise specified, we show all uncertainties at the 68% ( $1\sigma$ ) confidence level,

## 2 OBSERVATION AND DATA REDUCTION

### 2.1 Observation and Data Screening

We utilized the same *Suzaku* data (OBSID 903006010) of 1E 1547.0–5408 as used in Paper I, although short burst events were eliminated therein. The data were acquired over  $\sim 1$  day from 2009 January 28 21:34 (UT) to January 21:32 (UT). As described in Paper I, two (XIS1 and XIS3) among the three X-ray Imaging Spectrometer (XIS: Koyama et al. 2007) sensors were operated with a 1/4 window mode plus burst option, repeating a 0.5-sec exposure and a 1.5-s artificial dead-time. The other sensor, XIS0, was operated in the timing mode (P-sum mode) to attain a high time resolution of  $\sim 7.8$  ms together with one dimensional position information. The Hard X-ray Detector (HXD: Takahashi et al. 2007), composed of silicon PIN diodes (HXD-PIN; 10–70 keV) and GSO scintillators (HXD-GSO;  $\sim 50$ –600 keV), was operated in the normal mode with 61  $\mu\text{s}$  time resolution. Effective exposures were 42.5 ks, 10.6 ks, 10.6 ks, and 33.5 ks with XIS0, XIS1, XIS3, and the HXD, respectively.

Event screening criteria of the HXD are the same as Paper I except for two conditions. We allow all geomagnetic cutoff rigidity (which was  $\geq 6$  GV in Paper I), and any data transfer criteria, in order to include as many short bursts as

possible. These changes do not affect signal to noise ratios of short bursts, since they are almost free from the background due to their short duration ( $\lesssim 1$  s).

We utilized standard filtered files for XIS1 and XIS3, while started our XIS0 analyses from the unfiltered event file. These raw P-sum events were corrected and filtered in a way as recommended by the XIS team (Matsuta et al. 2010), including corrections of PI values by a ftool software *xispi*, selections with criteria of  $(\text{GRADE}==0\text{GRADE}==1\text{GRADE}==2) \ \&\& \ (\text{STATUS} >=0 \ \&\& \ \text{STATUS} <=524287)$ , and filtering with scripts of *xisrepro.xco* and *xis\_mkf.sel*. We further eliminated apparent hot pixels from the XIS0 data, and corrected the P-sum mode timing for the known delay (31.2 ms in the present case) depending on the source location on the CCD chip.

Figure 2 shows light curves of 1E 1547.0-5408 recorded with XIS0 (2–10 keV), XIS1+XIS3 (2–10 keV), HXD-PIN (10–70 keV), and HXD-GSO (50–150 keV), which exhibit background-inclusive average count rates of 3.89, 5.77, 0.76, and 13.38 counts  $\text{s}^{-1}$ , respectively. Several short burst events clearly appeared in all light curves.

## 2.2 Identification of Short Bursts

The short bursts are characterized as bunched X-ray photons. In order to identify such bunched events, we hence studied distributions of delta-time ( $\Delta t$ ), which is defined as waiting times of individual X-ray photons (including background events) from the preceding events. This study utilized the 10–70 keV HXD-PIN data, since they have a better signal to noise ratio than those of HXD-GSO and XIS0, and the finer time-resolution (61  $\mu\text{s}$ ) than XIS0 ( $\sim 7.8$  ms). Besides, unlike the XIS1 or XIS3 data with burst options, HXD-PIN is free from periodic data gaps. The  $\Delta t$  analysis provides a standard method to identify bunched events, and is actually implemented in the HXD digital electronics (HXD-DE; section 4.3 of Takahashi et al. 2007) to eliminate instrumental event bunching on time scales of  $\lesssim$  a few ms.

Figure 3a shows the calculated  $\Delta t$  distribution of the 10–70 keV HXD-PIN data with a bin size of  $t_{\text{bin}} = 7.8$  ms. A large portion of these events are non X-ray backgrounds (NXB). The  $\Delta t$  values of such random events follow an exponential probability distribution,  $P(\Delta t) \propto \exp(-\lambda\Delta t)$ , where  $\lambda$  is the average event rate. The best-fit exponential function, shown therein by a dash-dotted line, gives  $\lambda = 0.778 \pm 0.001$  count  $\text{s}^{-1}$ , which agrees well with the average count rate, 0.76 count  $\text{s}^{-1}$ , derived in §2.1. On closer inspection of Figure 3(a2), the actual  $\Delta t$  distribution deviates from the best fit model below  $\sim 50$  ms. This indicates that some events are bunched, with separations much shorter than  $\lambda^{-1}$ . Thus, we choose a threshold interval as  $\Delta t_{\text{th}} \equiv 6 t_{\text{bin}} = 46.9$  ms to regard an event as possibly bunched. The chance probability of observing  $\Delta t \leq \Delta t_{\text{th}}$  is  $\{1 - \exp(-\lambda\Delta t_{\text{th}})\} = 3.6\%$ .

Under the above preparation, we define “an event train of length  $N_{\text{bst}}$ ” as an event bunching where  $N_{\text{bst}}$  consecutive events are detected all with a waiting time of  $\Delta t < \Delta t_{\text{th}}$ . Most NXB events sparsely occur with  $\Delta t > \Delta t_{\text{th}}$ , and hence, with  $N_{\text{bst}}=0$ . Since the chance occurrence of a bunching with length  $N_{\text{bst}}$  is simply  $(0.036)^{N_{\text{bst}}}$ , we estimate those with  $N_{\text{bst}}=3, 4,$  and  $5$  as  $4.7 \times 10^{-5}$ ,  $1.7 \times 10^{-6}$ , and  $6.0 \times 10^{-8}$ , respectively. Considering the 10–70 keV total PIN events of  $\sim 3.4 \times 10^4$  counts, chance detections of event trains with

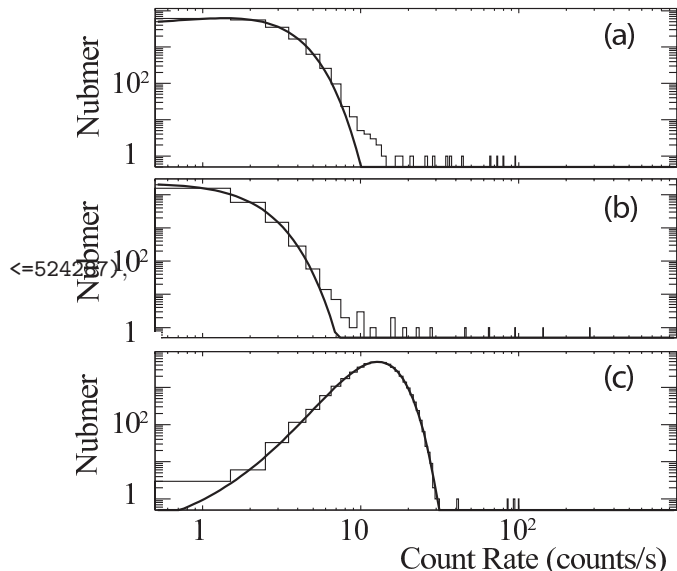


**Figure 4.** Distributions of 1-sec count rates for the XIS1+3 (panel a), HXD-PIN (panel b), and HXD-GSO (panel c) data. Best-fit Poisson distributions are also shown.

$N_{\text{bst}}=3, 4,$  and  $5$  during the entire observation become  $\sim 2$ ,  $\sim 0.06$ , and  $\sim 0.002$ , respectively. Therefore, event trains with  $N_{\text{bst}} \geq 4$  would be securely identified as short bursts. Compared to a more conventional way of detecting sudden increases in the light curve, this method is more suited to our search for weak bursts on two points; it is unaffected by count binning, and it works even when a burst has rather gradual rise (e.g., with a precursor).

Figure 3b shows the  $N_{\text{bst}}$  distribution in comparison with the predicted chance coincidence probability of ordinary events,  $(0.036)^{N_{\text{bst}}}$ . We find data points with  $N_{\text{bst}} \geq 4$  which are significantly deviated from the fit, and hence regard them as short bursts. We further merged two separate bursts into one if they were detected within the adjacent 1 sec. Using these criteria, we successfully detected 18 short burst events as listed in Table 1.

To confirm these detections in an independent way, we also studied distributions of the count rates in the light curves of Figure 2. The calculated histograms are shown in Figure 4. In Figure 4(b), the short bursts appear as significant deviations from the best-fit Poisson distribution, which is superposed as a solid curve. Even only from Figure 4(b), fifteen among the above eighteen bursts were recognized as those 1-sec bins where  $\geq 8$  events were detected. Thus, both methods give almost the same detections. Further corrections for the XIS1 timing mode are described in Appendix.A.

We also searched the Swift/BAT data for possible detections of the same short bursts. Using the same trigger code as used in Graziani (2003) on the 64 msec BAT data, only 2 bursts were recorded by the BAT. This is mainly because the BAT, with its wide field of view, has higher background. In other words, HXD-PIN onboard *Suzaku* has a far higher sensitivity to weak short bursts, as long as the source is inside its tightly collimated field of view. Therefore, we utilize the above *Suzaku* data set for the following analyses.

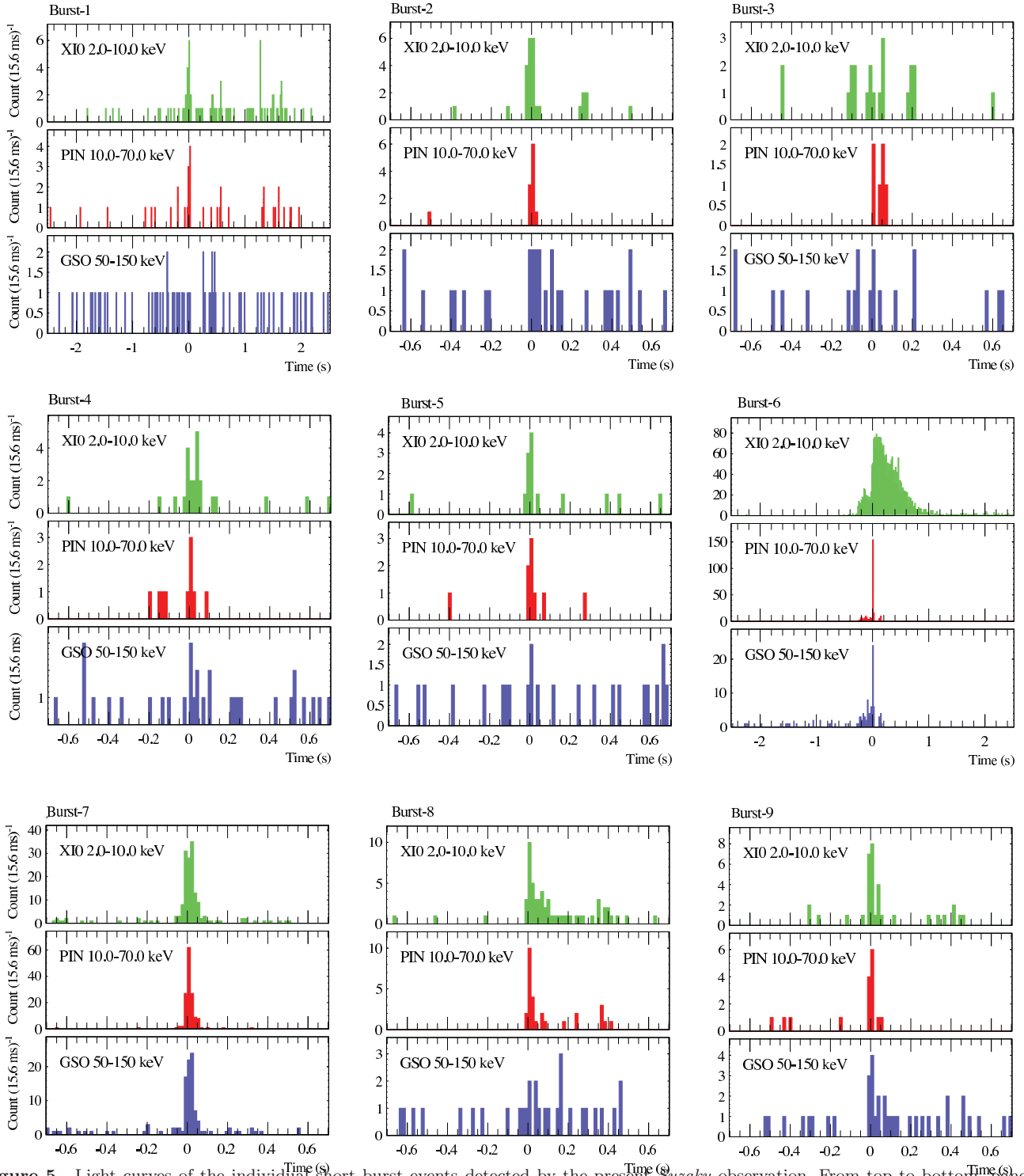


**Figure 5.** Light curves of the individual short burst events detected by the present *Suzaku* observation. From top to bottom, panels refer to those obtained with XIS0, with HXD-PIN, and with HXD-GSO, in the 2–10, 10–70, and 50–150 keV respectively. The time bin is 15.6 msec.

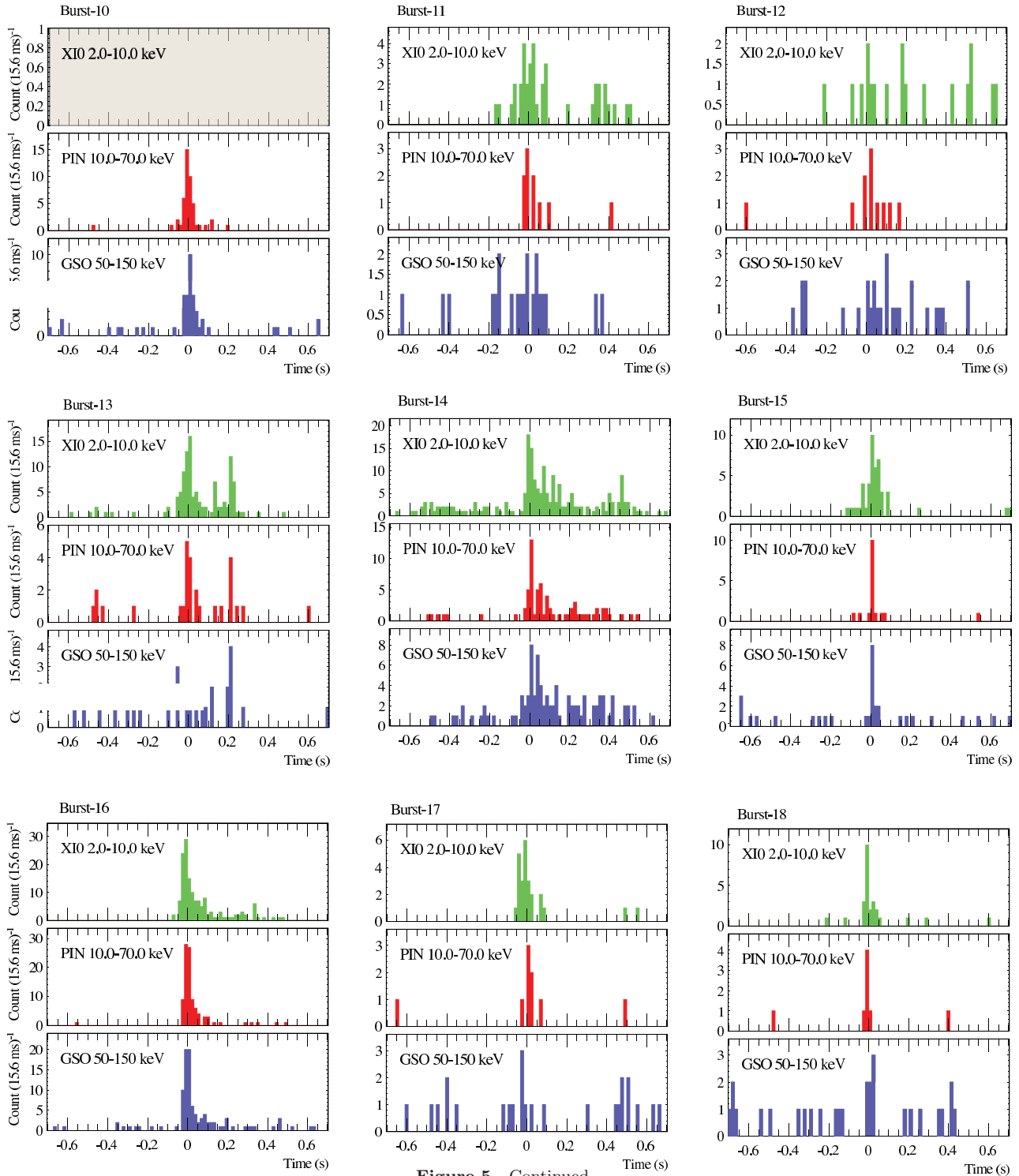


Figure 5. Continued.

### 3 ANALYSIS

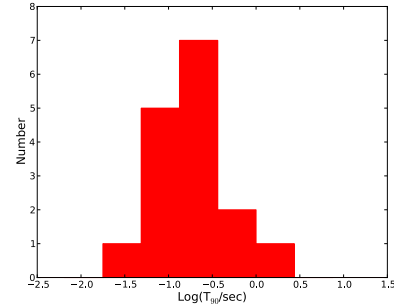
#### 3.1 Detected Bursts

Figure 5 shows the XIS, HXD-PIN, and HXD-GSO light curves of the bursts described in §2.2. Table 1 also gives their basic properties. The bursts are clearly detected by HXD-PIN and XIS0, and a considerable fraction of them by HXD-GSO as well. Due to the burst option, the coverage of these bursts with XIS1 and XIS3 (not shown in Figure 5) are highly incomplete. This however does not hamper our study, because we analyze below the XIS0 and HXD data of these bursts. We exclude Burst-6, presumably the strongest one, since a part of the HXD data was lost due to saturation of the data transfer. Likewise, Burst-10 is discarded, because it fell outside the good time interval (GTI) of the XIS. Thus, we hereafter analyze the remaining 16 short bursts. They are statistically significant with chance probabilities  $\lesssim 10^{-5}$  when combining the 1-sec data of XIS, HXD-PIN, and HXD-GSO together (Appendix. B; 1-sec rates are also shown in Table 1), and are free from data losses due to dead-time or pile-ups (Appendix C).

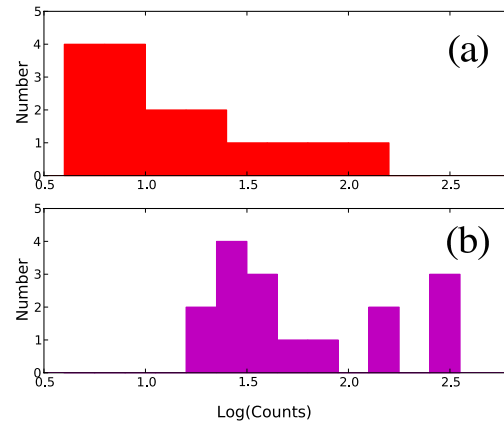
The burst peaks in Table 1 are defined as the time of the maximum count rate of HXD-PIN, which have higher signal-to-noise ratios than the others. As can be seen in Figure 5, these peaks can be determined with a typical uncertainty of a few bins, or  $\lesssim 50$  ms. Taking a closer look at individual light curves in Figure 5, some burst photons apparently appear outside the duration of  $N_{\text{bst}}$  (Table 1) defined in §2.2. Thus, using the XIS0 (2–10 keV) and HXD-PIN (10–70 keV) data co-added together, we manually defined tentative burst durations to cover whole possible burst X-ray photons. Within the above durations, we further calculated the time period,  $T_{90}$ , starting when 5% of the XIS0+PIN photons has been detected and ending when 95% has been observed. As shown in Figure 6 (and also Table 1), the  $T_{90}$  values range from  $\sim 47$  ms to 1.9 s, with the average of 321 ms. This value is close to the mean values derived in recent works of the same object,  $T_{90} = 258$  ms (van der Horst et al. 2012) and 305 ms (Scholz & Kaspi 2011), where the disagreement may have arisen because these works utilized different sets of short bursts, with different fluences and different energy ranges.

Figure 7 represents distributions of burst photon counts  $N_{T_{90}}$  detected during  $T_{90}$ . Thus,  $N_{T_{90}}$  of the 10–70 keV PIN data are distributed from  $\sim 5$  to  $\sim 130$ . Although  $N_{T_{90}}$  is sometimes slightly different from  $N_{\text{bst}}$  by up to  $\sim 50\%$ , the difference is negligible in the following analyses.

For spectral analyses of the individual bursts, the XIS0 and the HXD events accumulated over  $T_{90}$  were utilized as source spectra. The background of XIS0 was extracted using actual events on the CCD chip far away from the source position. The HXD-PIN background was not subtracted, since the average background rate ( $\sim 0.8$  Hz in 10–70 keV) implies at most  $\sim 1$  photon in  $T_{90}$ . On the other hand, for the HXD-GSO analyses, we produced the background spectra from the simulated GSO events (Fukazawa et al. 2009) during a 20 sec period around the corresponding burst, and subtracted them after scaling to the duration of  $T_{90}$ . The GSO background typically contains  $\sim 8$  counts per bursts, which amount to  $\sim 30\%$  of the signal counts. Although we did not produce background from the actual GSO data taken before/after the bursts to avoid possible contamination of the persistent or burst emission from the source, this alternative



**Figure 6.** Distribution of  $T_{90}$  for the 16 bursts determined from the 10–70 keV HXD-PIN data.



**Figure 7.** (a) Distribution of burst counts recorded over  $T_{90}$  in the 10–70 keV HXD-PIN data. (b) Same as panel (a), but for the total counts summed over the 2–10 keV XIS, 10–70 keV HXD-PIN, and 50–150 keV HXD-GSO data.

method gives consistent results. We employed standard response files (epoch 5) for the HXD, while used the response (rmf) and auxiliary response (arf) files for XIS0 produced as in §2.1.

The average fluxes and fluences of these bursts were estimated using a single PL model, with a column density of the photo-absorption fixed at  $N_{\text{H}} = 3.2 \times 10^{22} \text{ cm}^{-2}$  after Paper I. The resultant photon indices and the 10–70 keV X-ray fluxes are listed in Table 1. In some bursts, this PL model did not give an acceptable fit mainly due to a high energy signal deficiency. For such bursts, we alternatively utilized a cutoff power-law model (CutPL) with the same fixed photo-absorption. The 10–70 keV fluences integrated over  $T_{90}$  are also shown in Table 1. As one of the characteristics of the present burst sample, Figure 8 shows harness ratios of the bursts photons detected by the HXD to those by the XIS, as a function of their fluences. The fluences are distributed in the range of  $\sim 10^{-9}$ – $10^{-7} \text{ erg cm}^{-2}$ , and their hardness ratios ranges from  $\sim 0.4$  to  $\sim 3$ . Although a hardening trend towards weaker bursts was reported from SGRs (Gögüş et al. 2001), and a softening trend was reported from AXPs (Gavril et al. 2004), the present sample in Figure 8

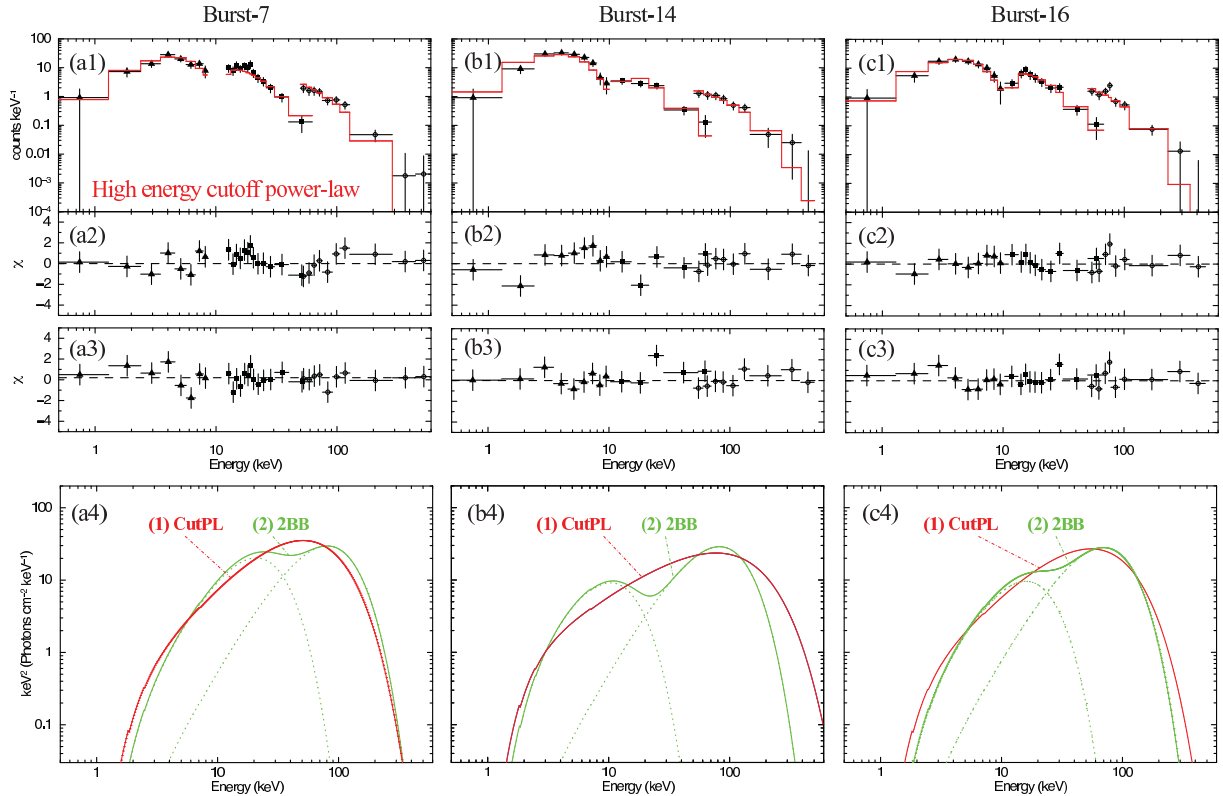


**Figure 9.** X-ray spectra of the three brightest bursts in our sample; Burst-7 (panels a1-a5), Burst-14 (panels b1-b5), and Burst-16 (panels c1-c5). Raw count spectra with XIS0, HXD-PIN, and HXD-GSO are shown in panel (1) with the best-fit CutPL model, and corresponding residuals are shown in panel (2). Panels (3) are residuals when the data are fitted by the 2BB model. Panels (4) are comparisons among the inferred best-fit CutPL (red) and 2BB (green) models. The spectra are shown after multiplied by individual  $T_{90}$  values. The XIS0 and HXD-GSO background were subtracted as described in §3.1.

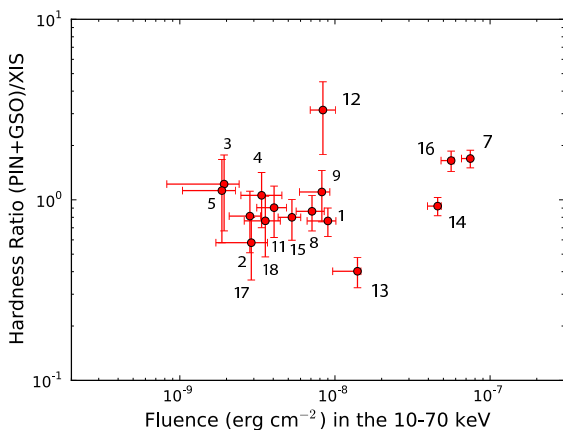


**Figure 8.** Hardness ratios of the detected X-ray photons  $N_{T90}$  during  $T_{90}$  calculated as  $(\text{PIN}+\text{GSO})/\text{XIS0}$ , as a function of the 10–70 keV fluence. Numbers in the figure indicate the corresponding burst ID.

does not show any significant corrections between the hardness and fluence.

Among the above 16 short bursts, we selected, for our detailed spectral analyses, three outstandingly bright ones, Burst-7, 14, and 16, which all satisfy  $N_{\text{bst}} \geq 60$  and show

fluences above  $2 \times 10^{-8} \text{ erg s}^{-1}$  (Figure 8). Although these are the brightest bursts among the present sample (except for Burst-6 which was discarded), they are still weaker compared to most of the bursts used in previous studies, of which the fluences are typically  $\sim 10^{-8}$ – $10^{-4} \text{ erg cm}^{-2}$ . Below we apply several spectral modelings to these bursts in the  $\sim 1$ – $300 \text{ keV}$  energy range. For all models, the column density for photo-absorption is fixed at  $N_{\text{H}} = 3.2 \times 10^{22} \text{ cm}^{-2}$  as before, unless otherwise noted. The normalization factor of XIS0 to the HXD was fixed at 1.08 based on the correction as described in §A2, although allowing it to float has an insignificant effect on the following results.

The single PL model with the fixed  $N_{\text{H}}$  gave acceptable fits to none of the three bursts, with reduced  $\chi^2_{\nu}$  values of 4.92, 2.83 and 3.89, for Burst-7, 14, and 16, respectively. Even if we make  $N_{\text{H}}$  free, the fits were still unacceptable ( $\chi^2_{\nu} \sim 2$ ). Discrepancies of these fits originate from model excess in the lowest and highest spectral ends. An optically thin bremsstrahlung model is not successful either ( $\chi^2_{\nu} > 2$ ). Then, we fitted these spectral data using the CutPL model, and obtained acceptable fits as summarized in Table 2 and in Figure 9. The fits yielded a photon index of  $\Gamma \sim 0.1$ – $0.8$  and a cutoff energy of  $E_{\text{cut}} \sim 27$ – $66 \text{ keV}$ . As alternative models, we utilized a two blackbody model (2BB). As shown in Table 2, it was also successful on the three bursts, and yield the lower and higher temperatures of 35 keV and 1820 keV, respectively.



In Figure 9 (a4), (b4) and (c4), the above two best-fit spectral models (the CutPL and 2BB) are compared in  $\nu F_\nu$  forms. They give relatively similar spectral shapes, except in the higher energy range above  $\sim 100$  keV where the models become unconstrained. In both models, spectral peaks appear in the HXD-PIN band ( $\sim 50$ – $100$  keV). Employing conventionally the CutPL model, absorption-corrected 0.2–300 keV fluences of Burst-7, Burst-14, and Burst-16, are obtained as  $1.1 \times 10^{-7}$ ,  $9.3 \times 10^{-8}$ , and  $8.7 \times 10^{-8}$  erg  $\text{cm}^{-2}$ , respectively. The fluence becomes  $\sim 4$ – $8 \times 10^{-8}$  erg  $\text{cm}^{-2}$  if calculated in the 10–70 keV band.

In Figure 10a, we compare the spectrum of the brightest Burst-7 with the persistent X-ray spectrum recorded during the same observation (Paper I). While the persistent spectrum is apparently composed of two components, the burst spectrum is more curved, without apparent evidence for such two-component nature.

### 3.2 Weak short bursts

As shown in Figure 8, the remaining 13 short bursts have considerably lower 10–70 keV fluences than the three studied above, distributed below  $2 \times 10^{-8}$  erg  $\text{cm}^{-2}$ . They have poorer statistics, and also tend to show similar harness ratios around  $\sim 1.0$ . Therefore, we have stacked their spectra together for detailed analysis, with accumulated total exposure of 3.7 sec. In order to justify the stacking procedure, we took spectral ratios of each burst to the stacked one, to find that the ratios can be fitted in each case successfully by a constant with a reduced chi-square of  $\lesssim 1.0$ . Therefore, the 13 bursts are concluded to have consistent spectral shapes, and hence the stacking procedure can be justified. The derived 13 constant ratios are distributed from 0.55 to 3.3, with the average and standard deviation of 1.56 and 1.05, respectively. This distribution, ranging by a factor of 6, agrees with that of the fluence shown in Figure 8. The analysis here utilized the same responses as those of the brighter three short bursts, and in the same way as the previous analyses; the background was subtracted from the XIS0 and HXD-GSO data.

Figure 11 shows a stacked light curve of these weaker short bursts accumulated with reference to their peak times. Thus, the burst emission is highly significant even in the HXD-GSO band. Figure 12a shows the raw spectrum of this cumulative weak-burst data after the background subtraction. Its average 10–70 keV flux is by an order of magnitude lower than those of the three brightest ones. The HXD-GSO background becomes comparable to the signal level around  $\sim 130$  keV, and we can claim the HXD-GSO detection at least up to 150 keV at  $2.8\sigma$ .

As summarized in Table 3, a PL model with the fixed  $N_{\text{H}}$  failed to give an acceptable fit ( $\chi_\nu^2 \sim 2.1$ ; Figure 12b), while a PL with free  $N_{\text{H}}$  was more successful ( $\chi_\nu^2 \sim 1.3$ ), yielding  $\Gamma = 1.57 \pm 0.04$  and  $N_{\text{H}} = 5.4_{-0.5}^{+0.8} \times 10^{22}$   $\text{cm}^{-2}$  (Figure 12c). In order to further improve the fit especially in higher energy range, we again tried the CutPL and 2BB fits with the same column density fixed at  $N_{\text{H}} = 3.2 \times 10^{22}$   $\text{cm}^{-2}$ . As summarized in Table 3 and shown in Figure 12d, the CutPL model gave an acceptable fit ( $\chi_\nu^2 \sim 0.8$ ) with  $\Gamma = 1.03 \pm 0.07$  and  $E_{\text{cut}} = 62.9_{-10.8}^{+14.5}$  keV, implying a mild spectral curvature. Since  $\Gamma$  and  $E_{\text{cut}}$  couple with each other, we show in Fig. 13 the fit confidence contours on the  $\Gamma$

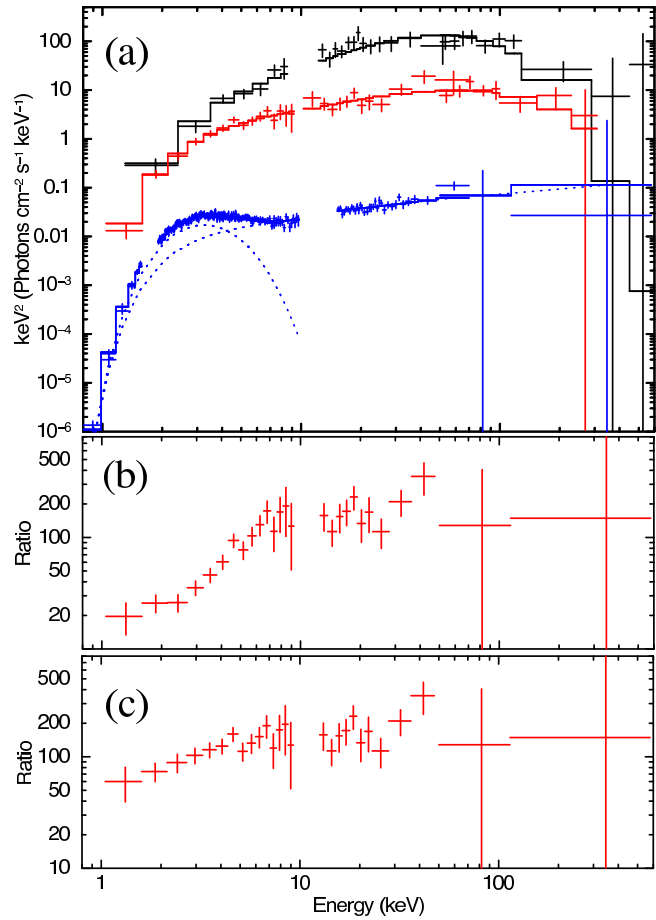


**Figure 10.** (a) Comparison of X-ray spectra of 1E 1547.0–5408 in  $\nu F_\nu$  forms. Top (black), middle (red), and bottom (blue) spectra represent Burst-7, the accumulated weak short bursts, and the persistent emission from Paper I, respectively. The CutPL model was employed to deconvolve the Burst-7 (Table 2) and the accumulated weak-burst spectra (Table 3), while a PL plus a BB for the persistent emission. The column density of the photo-absorption was fixed at  $3.2 \times 10^{22}$   $\text{cm}^{-2}$  in all cases. (b) The ratio between the red and blue spectra in panel (a). (c) Same as panel (b), but after eliminating the BB component from the persistent emission.

vs.  $E_{\text{cut}}$  plane. In contrast to the successful CutPL model, the more convex 2BB model, which was successful on the brightest three bursts (§3.1), became much less successful ( $\chi_\nu^2 \sim 1.6$ ; Figure 12e). Thus, the weaker bursts are considered to have a flatter 10–70 keV HXD-PIN spectrum than the brightest bursts, particularly Burst 7 and 16.

To make the above spectral difference clearer, we added this stacked weak bursts to Figure 10a in  $\nu F_\nu$  form, where we employed the CutPL model for deconvolution in the same way as Burst-7. The weaker bursts are by  $\sim 2$  orders of magnitude brighter than the persistent emission, and by  $\sim 1$  order of magnitude fainter than Burst 7. As visualized by this plot, the cumulative burst shows a hard X-ray spectrum which is less curved than that of Burst 7 and is similar to that of the persistent X-rays. In fact, the value of  $\Gamma_{\text{bst}} = 1.57 \pm 0.04$ , obtained above by the PL fit with free  $N_{\text{H}}$ , is consistent with  $\Gamma_{\text{per}} = 1.54_{-0.04}^{+0.03}$  of the persistent hard component (Table 3). Although the CutPL model gave

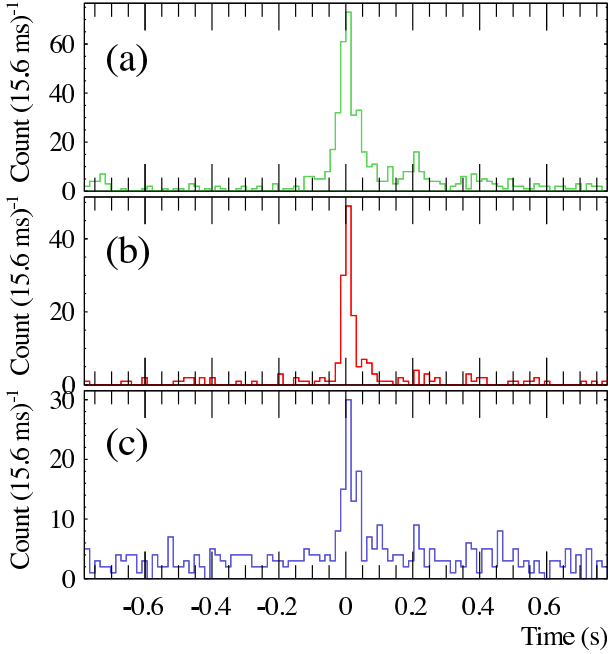


**Figure 11.** Light curves obtained by stacking the 13 weaker short bursts, with XIS0 (panel a), HXD-PIN (panel b), and HXD-GSO (panel c), in the 2–10, 10–70, and 50–150 keV band, respectively.

a much harder photon index,  $\Gamma_{\text{bst}} = 1.03 \pm 0.07$ , the slope is still similar, if considering the effect of cutoff around  $\sim 63$  keV.

In order to more directly compare these  $\nu F_\nu$  spectra, we divided the stacked weak-burst spectrum by that of the persistent emission. As shown in Figure 10b, the resultant ratios stay constant at  $\sim 170$  over the  $\sim 8$ –200 keV energy range. The remaining difference in the ratio below  $\sim 8$  keV in Figure 10b is thought to originate mainly from the presence of the soft BB component. We hence re-calculated the same ratio in Figure 10c after eliminating the soft BB component from the persistent spectrum. Thus, the ratio became much flatter even in energies below  $\sim 10$  keV, suggesting that the weak-burst spectrum is similar in shape to the hard X-ray component in the persistent emission.

Finally, in order to examine our weak-burst sample for its homogeneity, we subdivided the 13 bursts rather randomly into two subsets, under a constraint that they should be comparable, to within 10% in the summed signal photon counts (XIS0, PIN, GSO summed). From the two subsets, we then produced two stacked spectra instead of one, and analyzed them in the same manner as before. The pair of CutPL parameters obtained in this way are indicated in Figure 13 by a pair of data points with the same symbol. By

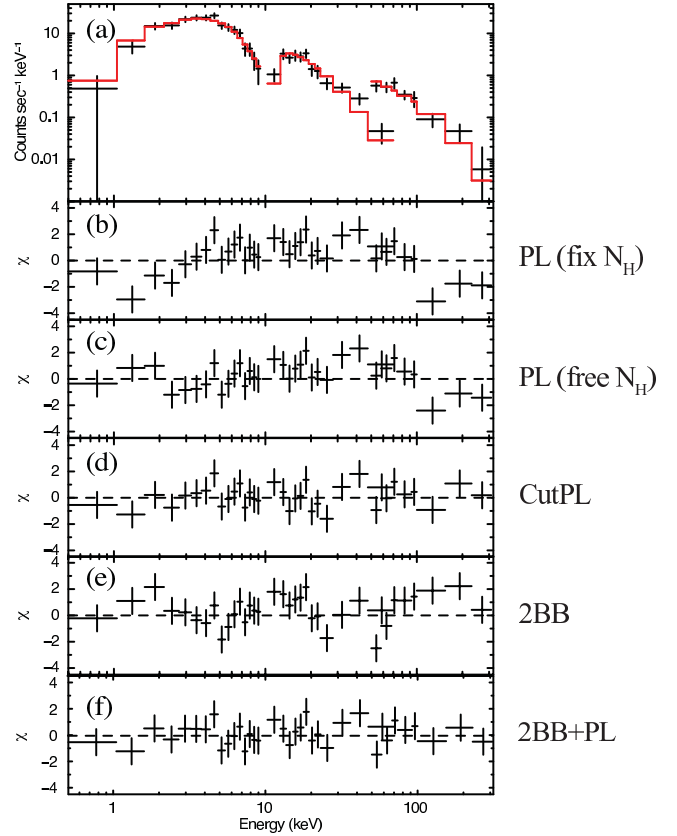


**Figure 12.** (a) Background-subtracted and response-inclusive spectra of the stacked weak bursts from 1E 1547.0–5408, compared with the best fit CutPL model (Table 3). Panels (b)–(f) show residuals when using a PL model with the fixed column density, a PL with the column density left free, a CutPL model, a 2BB model, and a 2BB+PL model, respectively.

trying six different partitions, we confirmed that the two subsets always give, within errors, consistent model parameters, which in turn are also consistent with those derived from the entire sample (indicated by contours). Therefore, the present sample can be regarded, within errors, as homogeneous.

### 3.3 Fitting by thermal/non-thermal components

Let us further examine the suggestion of Figure 10 that the burst emission has the same spectral components as the persistent X-ray emission. Especially the good similarity above  $\sim 8$  keV points to possible presence of the hard PL component in the stacked weak-burst spectrum, like in the persistent emission spectra. The short bursts from the transient magnetar SGR 0501+4516 were already examined for such a possibility with an affirmative answer (Nakagawa et al. 2011).

In order to assess the above consideration, we re-analyzed the stacked weak-burst spectrum, by adding, to the 2BB model, a hard PL with its slope fixed at  $\Gamma_{\text{per}} = 1.54$  as specified by the persistent emission (Paper I). The inclusion of the hard PL has made the 2BB fit acceptable, as summarized in Figure 12f and Table 3. The additional PL contributes to the total 1–300 keV flux by 52%, and is sta-

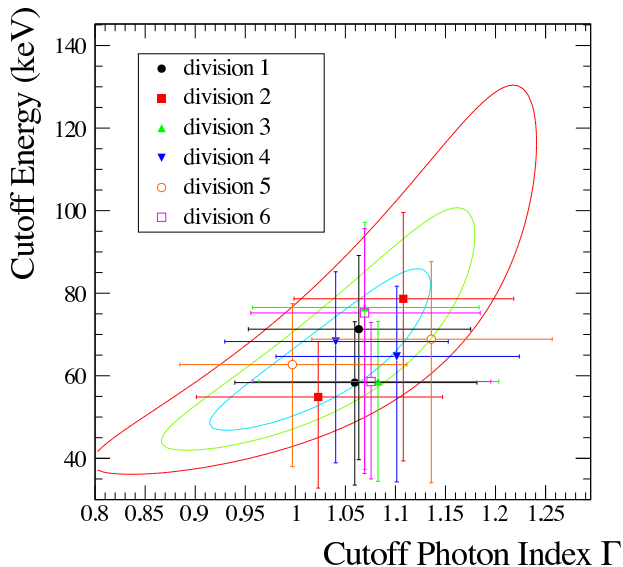


**Figure 13.** Confidence contours at the 68% (light blue), 90% (green), and 99% (red) confidence levels of the CutPL (panel a) fit to the stacked weak short burst spectrum. Individual data points show the parameters, with  $\pm 1\sigma$  errors, when the 13 short bursts are divided into two groups in six different ways.

tistically significant, because the achieved fit improvement,  $\Delta\chi^2 = -27.1$ , implies an F-test chance probability of  $2.4 \times 10^{-7}$ . Even though an acceptable fit with a comparable goodness had already been obtained with the CutPL model, we consider the 2BB+PL modeling more appropriate, for the following two reasons. One is that this modeling has successfully explained the spectra of weak short bursts from SGR 0501+4516 (Nakagawa et al. 2011). The other is that the 2BB model has been regarded as a standard representation of short-burst spectra of a fair number of magnetars (Nakagawa et al. 2007b and references therein), so that our final model should also be based on it, rather than the CutPL model which in the present case is quite conventional.

Now that evidence for the PL component has been obtained in the stacked weak-burst spectrum, it would be a natural step to examine the brighter ones, Burst-7, 14, and 16, for the same possibility, even though their spectra were already represented successfully by the 2BB model. This is because the distinction between the brighter and fainter bursts in the present observation is purely technical, without particular reason to consider that the two groups have distinct nature. Then, to the 2BB model describing the 3 bright bursts, we added the hard PL with  $\Gamma_{\text{bst}}$  fixed at the same value. This improved the fit to Burst-7, 14, and 16, by  $\Delta\chi = -4.3$ ,  $-2.0$ , and  $-2.8$ , giving F-test probabilities of 0.60%, 7.4%, and 2.4%, respectively. Thus, the hard PL component is likely to contribute at least to Burst-7. The best fit spectra are shown in Figure 14 in  $\nu F_\nu$  forms, with the derived parameters in Tabel 2. The BB temperatures did not change within errors from those obtained in the previous pure 2BB modeling (§3.1), while the hard PL component was found to contribute to the total 1–300 keV fluxes of Burst-7, 14, and 16, by 10%, 14%, and 19% respectively.

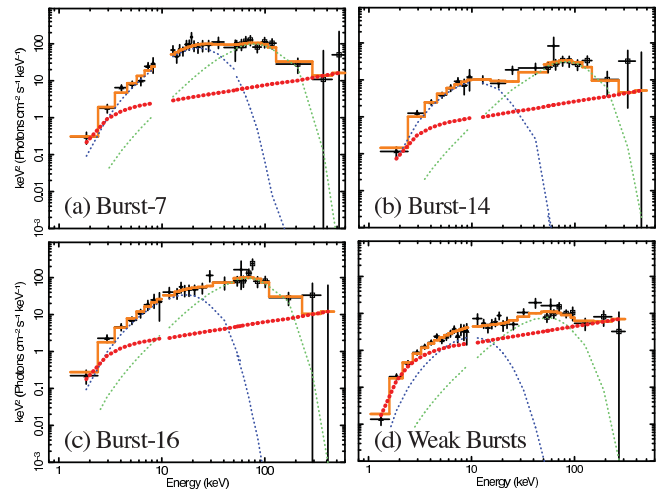


**Figure 14.** An  $\nu F_\nu$  presentation of the 2BB plus PL (with  $\Gamma = 1.54$  fixed) fits to the spectra of Burst-7 (panel a), Burst-14 (panel b), Burst-16 (panel c), and the stacked weak short bursts (panel d). The two BB components are represented in blue and green, while the hard PL in red.

## 4 DISCUSSION

### 4.1 Spectral comparison among different emissions

During the 33.5 ks of effective exposure with the HXD onto 1E 1547.0–5408 in its 2009 January activity, we detected 18 short bursts with their fluence  $S$  above  $S_{\text{min}} \sim 2 \times 10^{-9}$  erg  $\text{cm}^{-2}$ , and analyzed 16 of them. Even the strongest three among the 16 bursts, with the 10–70 keV fluence of  $S = 4\text{--}8 \times 10^{-8}$  erg  $\text{cm}^{-2}$  (or  $\sim 1 \times 10^{-7}$  erg  $\text{cm}^{-2}$  in 1–300 keV), are still weaker than most of previously reported bursts from magnetars in general which typically have  $S \gtrsim 10^{-7}$  erg  $\text{cm}^{-2}$ . For example, the burst forest of 1E 1547.0–5408 observed on 2009 January 22 with *Swift*, *INTEGRAL*, *Suzaku*, and *Fermi* was composed of events with  $S \gtrsim 2 \times 10^{-6}$  erg  $\text{s}^{-1}$  up to  $2.5 \times 10^{-4}$  erg  $\text{cm}^{-2}$  (Mereghetti et al. 2009). Therefore, the present *Suzaku* results, together with those by Nakagawa et al. (2011) on SGR 0501+4516, provide valuable information on the wide-band spectra of weak short bursts. For reference, the present sample defines a burst frequency of  $5.4 \times 10^{-4}$  burst  $\text{s}^{-1}$  in the range of  $S \gtrsim S_{\text{min}}$ .

So far, wide-band spectra of many energetic ( $S > 10^{-7}$  erg  $\text{s}^{-1}$ ) short bursts from magnetars have been explained successfully by the 2BB model: these include numerous bursts from SGR 1806–20 and SGR 1900+14 (Nakagawa et al. 2007b; Israel et al. 2008), as well as the strongest *Suzaku* burst from SGR 0501+4516 (Enoto et al. 2009; Nakagawa et al. 2011). At the same time, the 2BB model can generally reproduce the soft X-ray component, which is ubiquitously seen at energies of  $\lesssim 10$  keV of wide-band persistent spectra from magnetars (Mereghetti 2008) including 1E 1547.0–5408 itself (Paper I). These 2BB fits to the two different forms of magnetar emission reveal an interesting common scaling as  $T_{\text{Low}}/T_{\text{High}} \sim 0.4$  (Nakagawa et al. 2009), where  $T_{\text{Low}}$  and  $T_{\text{High}}$  denote the lower and higher 2BB temperatures, respectively. These results reinforce the possibility that the persistent emission is composed of numerous micro short bursts

(§1; Thompson & Duncan 1996; Lyutikov 2003; Nakagawa 2007a). Since the 2BB modeling is thus considered to have some physical meanings beyond a mere convention, below we construct our discussion based on the 2BB modeling, rather than those with the CutPL model which is rather empirical.

The three brightest bursts in our present sample, particularly the brighter two (Burst 7 and 16), among our sample exhibit upward convex spectral shapes, which have been successfully described by the 2BB model over an extremely wide energy band of  $\sim 1$  to  $\sim 300$  keV (§3.1). Importantly, the values of  $T_{\text{Low}}$  and  $T_{\text{High}}$  derived from these bursts (possibly except for Burst-14) obey the above scaling relation. In contrast, the stacked weaker bursts have a less convex shape (Figure 10), and did not accept the simple 2BB modeling. This is understandable if we presume that the spectra of weaker bursts are contributed by the hard component with a power-law photon index  $\Gamma \sim 1$ , which is generally observed in the persistent emission of magnetars (Kuiper et al. 2006; Enoto et al. 2010c). The weak bursts from SGR 0501+4516, when stacked together, actually exhibited a hard-tail feature (Nakagawa et al. 2011). In fact, Figure 10 b and c provide supporting evidence for this possibility, where the ratios become flatter above  $\sim 8$  keV. We have accordingly added a hard PL component to the 2BB model in §3.3, fixing  $\Gamma$  at the same value as obtained from the persistent emission, and obtained a fully acceptable spectral fit. Thus, the hard component is significantly present in the stacked weak-burst spectrum, as long as the 2BB model is chosen as the start point of analysis. As a further justification of this 2BB+PL modeling, the stacked spectrum yield  $T_{\text{High}}/T_{\text{Low}} = 4.9 \pm 1.1$  (from Table 3) in agreement with the "canonical" ratio, with it was  $7.3 \pm 0.5$  before properly including the PL component.

As argued by Nakagawa et al. (2011), these strengthen the similarity between the burst and persistent emissions. The report by Israel et al. (2008), that weaker bursts tend to show harder spectra in terms of the 2BB analysis, may be understood if considering possible contributions of the same PL component to their weaker bursts.

The above results have lead us to a natural question about brighter short bursts, of which the spectra generally lack the PL component: is this an intrinsic effect due, e.g., to some changes in the emission mechanism, or an artifact caused by their higher 2BB temperatures which mask any PL emission? With this in mind, we examined (§3.3) the spectra of the three brighter *Suzaku* bursts, for possible contribution from such a hard component. Then, the presence of the PL component (on top of the 2BB model) was suggested in Burst-7 at a relatively high confidence ( $>97\%$ ) level. The results are presented in Figure 15 on the thermal (2BB) vs non-thermal (PL) luminosity plane, in comparison with the weak-burst and persistent spectra. There, assuming a source distance of 4 kpc (Tiengo et al. 2010), the persistent X-ray emission (Paper I) is represented by a bolometric blackbody luminosity of  $L_{\text{BB}} = 1.2 \times 10^{35}$  erg  $\text{s}^{-1}$  and absorption-corrected 1–300 keV PL luminosity of  $L_{\text{PL}} = 6.9 \times 10^{35}$  erg  $\text{s}^{-1}$ , which sum up to give the total luminosity of  $L_{\text{per}} = 8.1 \times 10^{35}$  erg  $\text{s}^{-1}$ . We also quote the results on SGR 0501+4516, taken from Nakagawa et al. (2011). Although it is still difficult at present to distinguish the two alternatives the PL luminosity, if it is universally present in short bursts, appears to saturate at  $\sim 10^{38}$  erg  $\text{s}^{-1}$ , preferring the former possibility.

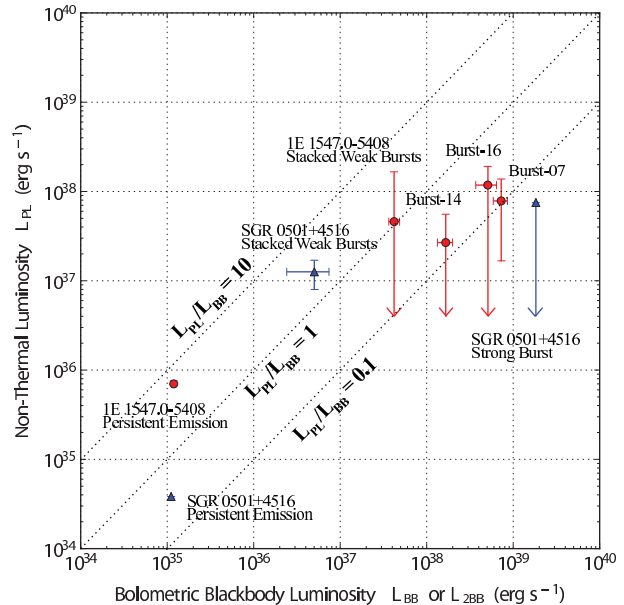


**Figure 15.** Comparison of the 1–300 keV PL luminosity to the bolometric BB luminosity. The results on SGR 0501+4516 were taken from Figure 8 in Nakagawa et al. (2011). In this plot, errors are shown at the 90% C.L. level.

On large scales, Figure 15 reveals a clear positive correlation between luminosities of the two emission components. Therefore, the soft (thermal) and hard (PL) components are considered to approximately keep their luminosity ratio over a very broad scale in flux or fluence. Similarly, Enoto et al. (2010c) showed that the luminosity ratio between these two emission components, comprising the persistent emission, is not much different between magnetars in activity and those in quiescence. These facts give another support to the microburst conjecture.

## 4.2 LogN-logS relation of short burst

In order to examine the possibility that the persistent X-ray emission is composed of micro burst events, it is inevitable to evaluate X-ray fluxes accumulated over resolved and unresolved bursts events. Since the present short bursts, with  $S \gtrsim S_{\text{min}} \sim 2 \times 10^{-9}$  erg  $\text{cm}^{-2}$ , were detected at a low burst frequency,  $5 \times 10^{-4}$   $\text{s}^{-1}$ , their accumulated flux is still at a level of  $\sim 10^{-12}$  erg  $\text{s}^{-1}$   $\text{cm}^{-2}$ . This is by  $\sim 2$  orders of magnitude lower than the observed persistent X-ray flux. Therefore, much larger contributions of smaller unresolved short bursts are required to explain the persistent X-ray flux.

For a quantitative estimate, let  $N(>S)$  denote the occurrence frequency of those bursts of which the fluence is  $>S$ . Observationally,  $N$  is thought to be described by a single power-law as  $N(>S) \propto S^{-\alpha}$ , like in solar flares and earthquakes. Sometimes known as the Gutenberg-Richter law, this relation is considered to represent self-organized criticality. Previous observations of SGR 1806–20 gave a range of  $\alpha = 0.7\text{--}1.1$ ; e.g.,  $\alpha \sim 0.9$  by the *Konus-Wind* (Aptekar et al. 2001),  $\alpha = 0.76 \pm 0.17$  by the BATSE,  $\alpha = 0.67 \pm 0.15$  by ICE (Gögüş et al. 2000),  $\alpha = 0.91 \pm 0.09$  by *INTEGRAL* (Götz et al. 2006), and  $\alpha = 1.1 \pm 0.6$  by *HETE-2* (Nakagawa et al. 2007b). From the present tar-

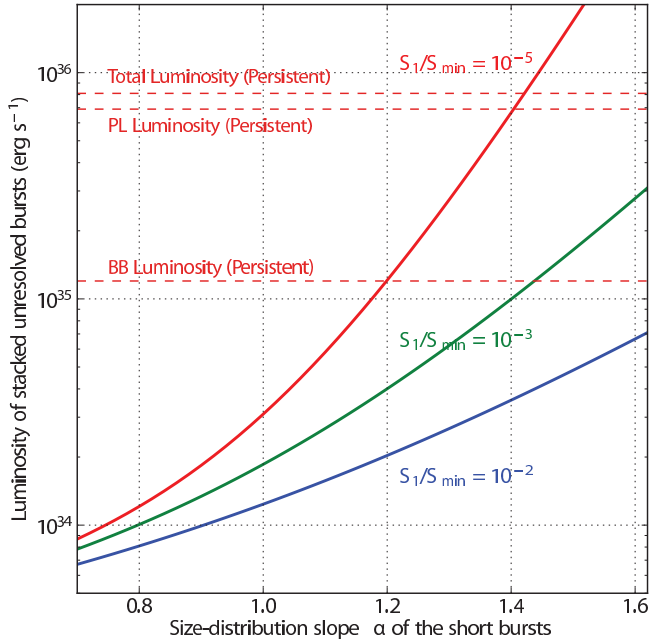


**Figure 16.** Expected luminosity of integrated unresolved weaker bursts, as a function of the size-distribution slope  $\alpha$ . Blue, green, and red lines are the calculations with the lower bounds of the integration at  $S_1/S_{\min} = 10^{-2}$ ,  $10^{-3}$ , and  $10^{-5}$ , respectively. Three horizontal lines represents the persistent X-ray luminosity of 1E 1547.0–5408 for the total (top), PL (middle), and BB (bottom) components.

get, 1E 1547.0–5408, the slope is reported to be  $\alpha = 0.75 \pm 0.06$  and  $\alpha = 0.6 \pm 0.1$  through *INTEGRAL*/ACS (Mereghetti et al. 2009) and *Swift*/XRT (Scholz & Kaspi 2011) observations, respectively.

The burst number density at a particular fluence  $S$  is written as  $f_{\text{bst}}(S) \propto -dN(S)/dS \equiv (f_0/S_0)(S/S_0)^{-\alpha-1}$ , where  $S_0$  is a typical fluence and  $f_0$  (burst  $\text{s}^{-1}$ ) is a normalization constant. Thus, the luminosity integrated over bursts between  $S_1$  and  $S_2$ , at a distance  $d$  (kpc), is given as

$$\begin{aligned} L_X &= \int_{S_1}^{S_2} 4\pi d^2 S f_{\text{bst}}(S) d(S) \\ &= 4\pi d^2 S_0 f_0 \int_{s_1}^{s_2} s^{-\alpha} ds \\ &= 4\pi d^2 S_0 f_0 (s_2^{1-\alpha} - s_1^{1-\alpha}) / (1-\alpha), \end{aligned}$$

with  $s \equiv S/S_0$ ,  $s_1 \equiv S_1/S_0$ , and  $s_2 \equiv S_2/S_0$ . Here, let us assume  $S_0 = S_{\min} \sim 2 \times 10^{-9}$  erg  $\text{cm}^{-2}$  (the present detection limit), and  $s_2 = S_2/S_{\min} = 1$ , at  $d = 4$  kpc. The observed frequency  $N(S_{\min}) \sim 5.4 \times 10^{-4}$  burst  $\text{s}^{-1}$  gives  $f_0 \sim 7 \times 10^{-4}$  burst  $\text{s}^{-1}$ . In order to explain the persistent luminosity in this way, we clearly need  $\alpha > 1.0$ , because  $S \times N \propto S^{1-\alpha}$  should increase towards smaller values of  $S$ . More quantitatively, Figure 16 shows the calculated value of  $L_X$  as a function of  $\alpha$  for these different values of  $s_1$ .

Comparing the three brightest bursts and the stacked weaker ones in Table 2 and Table 3, the blackbody radii of neither the lower- or higher-temperature components are strongly dependent on their fluences  $S$ . Thus, as a first-order approximation, let us assume  $S \propto kT^4$  after the Stefan-

Boltzmann law. Since the weak bursts with  $S_{\min}$  and persistent emission give  $kT_{\text{High}} \sim 12$  keV and  $kT \sim 0.65$  keV, respectively, a typical unresolved weakest burst is considered to have a fluence  $s_1 = S_1/S_{\min} \sim (0.65 \text{ keV}/12 \text{ keV})^4 \sim 10^{-5}$ . Combining with Figure 16, this implies that the slope  $\alpha$  should be  $\sim 1.2$  and  $\sim 1.4$  to supply the luminosity of the persistent BB and PL luminosities, respectively.

The required value of  $\alpha = 1.2$ – $1.4$  is larger than has been measured. Since the observations of bursts were performed mainly during more burst-active states than in the *Suzaku* observation, a possible interpretation is variations of  $\alpha$  depending on the magnetar activity. For example, the solar flare is known to change its size-distribution slope  $\alpha$ , from  $\sim 0.8$  at activity peaks to  $\sim 1.2$  in more quiescent states (Bromund et al. 1995). This is also pointed out in some magnetars (see also SGR 1806–20 and SGR 1900+14 in Nakagawa et al. 2007b, related with SGR 0501+4516 behavior in Göğüş et al. 2010). If  $\alpha$  reaches 1.2–1.4 in less burst-active states, the persistent emission can be explained by the superposition of micro bursts. Otherwise, an alternative dissipation process that is independent of the short-burst production is inferred to be also contributing to the persistent emission. Such processes include, e.g., internal crustal heating in magnetars (Aguilera et al. 2008).

### 4.3 Energy source for the emissions

Finally, let us compare energetics of the bursts and persistent emission with the magnetic energies of magnetars. Assuming 4 kpc as before, the 2BB model and the Stefan-Boltzmann law measure the total radiated energies of  $2.1 \times 10^{38}$  erg,  $1.6 \times 10^{38}$  erg, and  $1.6 \times 10^{38}$  erg, from Burst-7, Burst-14, and Burst-16, respectively. Further considering the  $T_{90}$  values, these yield bolometric luminosities of  $7.8 \times 10^{38}$  erg  $\text{s}^{-1}$ ,  $1.9 \times 10^{38}$  erg  $\text{s}^{-1}$ , and  $5.9 \times 10^{38}$  erg  $\text{s}^{-1}$ , respectively. In the weaker bursts, an average energy emitted per burst becomes  $1.2 \times 10^{37}$  erg, and the bolometric luminosity is  $4.2 \times 10^{37}$  erg  $\text{s}^{-1}$ .

In comparison with the above estimates, the magnetic energy stored within a size of  $R_{\text{mag}}$  becomes

$$\begin{aligned} E_{\text{bst}} &= \frac{B^2}{8\pi} R_{\text{mag}}^3 \text{ erg} \\ &= 2 \times 10^{45} \left( \frac{B}{B_{\text{surf}}} \right)^2 \left( \frac{R_{\text{mag}}}{R_{\text{NS}}} \right)^3 \text{ erg}, \end{aligned}$$

when normalizing to the dipole magnetic field,  $B_{\text{surf}} = 2.2 \times 10^{14}$  G (Camilo et al. 2007), and employing the canonical neutron star radius  $R_{\text{NS}} = 10$  km. If the individual burst emission is powered by dissipation of the magnetic energy in this region (e.g., via reconnection; Lyutikov 2006), a typical size of  $R_{\text{mag}} \gtrsim 10^{-2.3} R_{\text{NS}}$  is needed. Blackbody radii observed in our sample (the 2BB model),  $R_{\text{Low}} \sim 1$  km =  $0.1 R_{\text{NS}}$  and  $R_{\text{High}} \sim 0.1$  km =  $10^{-2} R_{\text{NS}}$ , are larger than the required  $R_{\text{mag}}$ . This is considered reasonable, because the released magnetic energy would in any case diffuse out, and would make  $R_{\text{BB}} > R_{\text{mag}}$ .

If we assume  $s_1 \sim 10^{-5}$  and  $\alpha \sim 1.4$  like in the previous subsection, the burst frequency at  $S_1$  is estimated to be  $f \sim 10^3$  Hz. Therefore, a minimum size of  $R_{\text{mag}}/R_{\text{NS}} \sim 10^{-4}$  is enough to supply the observed luminosity  $L_x \sim 6 \times 10^{35}$  erg  $\text{s}^{-1}$ , if the released magnetic energy is evaluated as  $L_{\text{mag}} \sim 2 \times 10^{45} (B/B_{\text{surf}})^2 (R_{\text{mag}}/R_{\text{NS}})^3 f$  erg  $\text{s}^{-1}$ . Since the

persistent emission exhibits  $R_{\text{BB}} \sim 5$  km (Paper I), the condition of  $R_{\text{BB}} > R_{\text{mag}}$  is retained.

## 5 CONCLUSION

We studied short bursts from 1E 1547.0–5408 (also known as SGR J1550–5418, PSR J1550–5418) detected during the *Suzaku* pointing observation on 2009 January 28–29 (UT) in its burst-active state. This period was 7 days after the burst forests on January 22. Combined with the previous study of its persistent X-ray emission (Paper I), we have obtained the following results.

(i) Using a  $\Delta t$  distribution of the HXD-PIN data, we identified 18 short burst events with its risk probability below  $\sim 1.7 \times 10^{-6}$ . Sixteen of them, free from the data loss, were used for the spectral analyses.

(ii) Three brightest bursts have their fluences of  $\sim 4\text{--}8 \times 10^{-8}$  erg cm $^{-2}$  in the 10–70 keV energy range. Their individual spectra were fitted successfully by the 2BB model (and some other models) over the 0.5–400 keV band.

(iii) Remaining 13 bursts define one of the weakest samples ever measured, with their fluences covering the range of  $2 \times 10^{-9}\text{--}2 \times 10^{-8}$  erg cm $^{-2}$ . Their stacked spectrum shows similarity to the persistent emission in its slope above  $\sim 8$  keV. This spectral similarity extends to even towards lower energies after eliminating the BB component from the persistent spectrum.

(iv) The stacked spectrum cannot be represented by a 2BB model, while an additional hard PL made the fit acceptable, even fixing the slope at the value of the persistent one. The luminosity of the hard PL shows a sign to saturate at  $\sim 10^{38}$  erg s $^{-1}$ , when compared to the thermal luminosity.

(v) We evaluated the available energy supplied from the unresolved short bursts. The persistent emission from 1E 1547.0–5408 can be explained if the slope  $\alpha$  of the cumulative distribution of the short bursts is rather steep as  $\alpha = 1.2\text{--}1.4$ .

We thank members of the *Suzaku* magnetar Key Project and the *Suzaku* operation teams for the successful ToO. TE is supported by the JSPS Postdoctoral Fellowships for Research Abroad.

## REFERENCES

- Aptekar, R. L., Frederiks, D. D., Golenetskii, S. V., Il'inskii, V. N., Mazets, E. P., Pal'shin, V. D., Butterworth, P. S., & Cline, T. L. 2001, *ApJS*, 137, 227
- Aguilera, D. N., Pons, J. A., & Miralles, J. A. 2008, *ApJL*, 673, L167
- Baring, M. G., & Harding, A. K. 2007, *Astrophysics and Space Science*, 308, 109
- Bellm, E., Smith, D. M., & Hurley, K. 2009, *GRB Coordinates Network*, 8857, 1
- Beloborodov, A. M., & Thompson, C. 2007, *Astrophysics and Space Science*, 308, 631
- Bernardini, F., et al. 2009, *Astronomy and Astrophysics*, 498, 195
- Bernardini, F., et al. 2011, arXiv:1102.5419
- Bromund, K. R., McTiernan, J. M., & Kane, S. R. 1995, *ApJ*, 455, 733
- Camilo, F., Ransom, S. M., Halpern, J. P., & Reynolds, J. 2007, *ApJL*, 666, L93
- Connaughton, V., & Briggs, M. 2009, *GRB Coordinates Network*, 8835, 1
- den Hartog, P. R., Kuiper, L., Hermsen, W., Kaspi, V. M., Dib, R., Knödlseeder, J., & Gavriil, F. P. 2008, *Astronomy and Astrophysics*, 489, 245
- den Hartog, P. R., Kuiper, L., & Hermsen, W. 2009, *The Astronomer's Telegram*, 1922, 1
- Duncan, R. C., & Thompson, C. 1992, *ApJL*, 392, L9
- Enoto, T., et al. 2009, *ApJL*, 693, L122
- Enoto, T., et al. 2010a, *ApJ*, 715, 665
- Enoto, T., et al. 2010b, *PASJ*, 62, 475
- Enoto, T., Nakazawa, K., Makishima, K., Rea, N., Hurley, K., & Shibata, S. 2010c, *ApJL*, 722, L162
- Enoto, T., Makishima, K., Nakazawa, K., Kokubun, M., Kawaharada, M., Kotoku, J., & Shibazaki, N. 2011, *PASJ*, 63, 387
- Esposito, P., Israel, G. L., Turolla, R., et al. 2011, *MNRAS*, 416, 205
- Fernández, R., & Thompson, C. 2007, *ApJ*, 660, 615
- Feroci, M., Hurley, K., Duncan, R. C., & Thompson, C. 2001, *ApJ*, 549, 1021
- Fukazawa, Y., et al. 2009, *PASJ*, 61, 17
- Gavriil, F. P., Kaspi, V. M., & Woods, P. M. 2004, *ApJ*, 607, 959
- Gelfand, J. D., & Gaensler, B. M. 2007, *ApJ*, 667, 1111
- Gögüş, E., Woods, P. M., Kouveliotou, C., van Paradijs, J., Briggs, M. S., Duncan, R. C., & Thompson, C. 2000, *ApJL*, 532, L121
- Gögüş, E., Kouveliotou, C., Woods, P. M., Thompson, C., Duncan, R. C., & Briggs, M. S. 2001, *ApJ*, 558, 228
- Gögüş, E., Woods, P. M., Kouveliotou, C., Kaneko, Y., Gaensler, B. M., & Chatterjee, S. 2010, *ApJ*, 722, 899
- Gögüş, E., Cusumano, G., Levan, A. J., et al. 2010, *ApJ*, 718, 331
- Golenetskii, S., Aptekar, R., Mazets, E., Pal'shin, V., Frederiks, D., Oleynik, P., Ulanov, M., & Cline, T. 2009, *GRB Coordinates Network*, 8863, 1
- Gotthelf, E. V., Halpern, J. P., Buxton, M., & Bailyn, C. 2004, *ApJ*, 605, 368
- Gotthelf, E. V., & Halpern, J. P. 2005, *ApJ*, 632, 1075
- Götz, D., et al. 2006, *Astronomy and Astrophysics*, 445, 313
- Graziani, C. 2003, *Gamma-Ray Burst and Afterglow Astronomy 2001: A Workshop Celebrating the First Year of the HETE Mission*, 662, 79
- Gronwall, C., Holland, S. T., Markwardt, C. B., Palmer, D. M., Stamatikos, M., & Vetere, L. 2009, *GRB Coordinates Network*, 8833, 1
- Halpern, J. P., Gotthelf, E. V., Becker, R. H., Helfand, D. J., & White, R. L. 2005, *ApJL*, 632, L29
- Halpern, J. P., Gotthelf, E. V., Reynolds, J., Ransom, S. M., & Camilo, F. 2008, *ApJ*, 676, 1178
- Heyl, J. S., & Hernquist, L. 2005, *MNRAS*, 362, 777
- Hurley, K., et al. 2005, *Nature*, 434, 1098
- Ibrahim, A. I., et al. 2004, *ApJL*, 609, L21
- Israel, G. L., et al. 2004, *ApJL*, 603, L97
- Israel, G. L., Campana, S., Dall'Osso, S., Munro, M. P., Cummings, J., Perna, R., & Stella, L. 2007, *ApJ*, 664,

- 448
- Israel, G. L., et al. 2008, *ApJ*, 685, 1114
- Israel, G. L., et al. 2010, *MNRAS*, 408, 1387
- Kaneko, Y., Gogus, E., Kouveliotou, C., Granot, J., Ramirez-Ruiz, E., & the GBM Magnetar Team 2010, arXiv:1001.2644
- Kargaltsev, O., Kouveliotou, C., Pavlov, G. G., et al. 2012, *ApJ*, 748, 26
- Kouveliotou, C., et al. 2001, *ApJL*, 558, L47
- Kouveliotou, C., von Kienlin, A., Fishman, G., Connaughton, V., van der Horst, A., & Bhat, N. 2009, *GRB Coordinates Network*, 8915, 1
- Koyama, K., et al. 2007, *PASJ*, 59, 23
- Kuiper, L., Hermsen, W., den Hartog, P. R., & Collmar, W. 2006, *ApJ*, 645, 556
- Kuiper, L., den Hartog, P. R., & Hermsen, W. 2009, *The Astronomer’s Telegram*, 1921, 1
- Lamb, R. C., & Markert, T. H. 1981, *ApJ*, 244, 94
- Lyutikov, M. 2003, *MNRAS*, 346, 540
- Lyutikov, M. 2006, *MNRAS*, 367, 1594
- Matsuta, K., et al. 2009, *Proceeding of the Suzaku Conference The Energetic Cosmos: from Suzaku to ASTRO-H*, 412
- Matsuta, K., Higashi, K., Tsujimoto, M., and the XIS team, 2010, “Recipe for reducing XIS data taken with the P-sum/timing mode”, [http://www.astro.isas.ac.jp/suzaku/analysis/xis/psum\\_recipe/Psum-recipe-20100724.pdf](http://www.astro.isas.ac.jp/suzaku/analysis/xis/psum_recipe/Psum-recipe-20100724.pdf)
- Mazets, E. P., Golentskii, S. V., Ilinskii, V. N., Aptekar, R. L., & Guryan, I. A. 1979, *Nature*, 282, 587
- Mereghetti, S. 2008, *The Astronomy and Astrophysics Review*, 15, 225
- Mereghetti, S., et al. 2009, *ApJL*, 696, L74
- Muno, M. P., Gaensler, B. M., Clark, J. S., de Grijs, R., Pooley, D., Stevens, I. R., & Portegies Zwart, S. F. 2007, *MNRAS*, 378, L44
- Nakagawa 2007a, Ph.D. Thesis, Aoyama Gakuin University
- Nakagawa, Y. E., et al. 2007b, *PASJ*, 59, 653
- Nakagawa, Y. E., Yoshida, A., Yamaoka, K., & Shibazaki, N. 2009, *PASJ*, 61, 109
- Nakagawa, Y. E., Makishima, K., & Enoto, T. 2011, *PASJ*, 63, S813
- Ng, C.-Y., et al. 2011, *ApJ*, 729, 131
- Olive, J.-F., et al. 2004, *ApJ*, 616, 1148
- Paczynski, B. 1992, *Acta Astron.*, 42, 145
- Rea, N., Turolla, R., Zane, S., Tramacere, A., Stella, L., Israel, G. L., & Campana, R. 2007, *ApJL*, 661, L65
- Rea, N., et al. 2009, *MNRAS*, 396, 2419
- Rea, N., Esposito, P., Turolla, R., et al. 2010, *Science*, 330, 944
- Rea, N., Israel, G. L., Esposito, P., et al. 2012, *ApJ*, 754, 27
- Savchenko, V., Beckmann, V., Neronov, A., Mereghetti, S., von Kienlin, A., Beck, M., Borkowski, J., & Gotz, D. 2009, *GRB Coordinates Network*, 8837, 1
- Scholz, P., & Kaspi, V. M. 2011, arXiv:1106.5445
- Sugizaki, M., Mitsuda, K., Kaneda, H., Matsuzaki, K., Yamauchi, S., & Koyama, K. 2001, *ApJS*, 134, 77
- Takahashi, T., et al. 2007, *PASJ*, 59, 35
- Terada, Y., et al. 2008, *PASJ*, 60, 25
- Terada, Y., et al. 2009, *GRB Coordinates Network*, 8845, 1
- Tiengo, A., et al. 2010, *ApJ*, 710, 227
- Thompson, C., & Beloborodov, A. M. 2005, *ApJ*, 634, 565
- Thompson, C., & Duncan, R. C. 1995, *MNRAS*, 275, 255
- Thompson, C., & Duncan, R. C. 1996, *ApJ*, 473, 322
- Thompson, C., Lyutikov, M., & Kulkarni, S. R. 2002, *ApJ*, 574, 332
- van der Horst, A. J., Connaughton, V., Kouveliotou, C., et al. 2010, *ApJL*, 711, L1
- van der Horst, A. J., Kouveliotou, C., Gorgone, N. M., et al. 2012, *ApJ*, 749, 122
- von Kienlin, A., & Connaughton, V. 2009, *GRB Coordinates Network*, 8838, 1
- Woods, P. M., & Thompson, C. 2006, *Compact stellar X-ray sources*, 547

**Table 1.** List of detected short burst events.

| ID | Time at Burst Peak<br>(UTC) | T90<br>(ms) | $N_{\text{bst}}^1$ | $N_{\text{T90}}^2$ | 1-sec Rate <sup>2</sup> | Model | Photon<br>Index         | Flux <sup>3</sup>    | Fluence <sup>3</sup> | $\chi^2_{\nu}$<br>(p-value) |
|----|-----------------------------|-------------|--------------------|--------------------|-------------------------|-------|-------------------------|----------------------|----------------------|-----------------------------|
| 1  | 2009-01-28T21:48:24.8       | 1851.4      | 9                  | (72, 26, 29)       | (37, 15, 25)            | PL    | $1.65^{+0.16}_{-0.13}$  | $0.5^{+0.1}_{-0.1}$  | $9.0^{+1.1}_{-2.4}$  | 1.09(0.36)                  |
| 2  | 2009-01-29T02:36:02.2       | 46.9        | 9                  | (16, 9, 4)         | (26, 10, 25)            | PL    | $1.34^{+0.13}_{-0.12}$  | $6.0^{+1.0}_{-1.6}$  | $2.8^{+0.5}_{-0.7}$  | 0.81(0.60)                  |
| 3  | 2009-01-29T03:06:21.3       | 148.4       | 5                  | (9, 4, 7)          | (20, 6, 14)             | PL    | $1.07^{+0.29}_{-0.25}$  | $1.3^{+0.3}_{-0.7}$  | $1.9^{+0.5}_{-1.1}$  | 0.75(0.69)                  |
| 4  | 2009-01-29T08:09:06.6       | 226.5       | 4                  | (17, 8, 10)        | (21, 10, 21)            | PL    | $1.24^{+0.12}_{-0.12}$  | $1.5^{+0.5}_{-0.4}$  | $3.4^{+1.2}_{-0.9}$  | 1.19(0.31)                  |
| 5  | 2009-01-29T08:53:23.4       | 78.1        | 5                  | (8, 5, 4)          | (12, 9, 14)             | PL    | $1.18^{+0.19}_{-0.17}$  | $2.4^{+0.5}_{-1.1}$  | $1.9^{+0.4}_{-0.8}$  | 0.44(0.82)                  |
| 6  | 2009-01-29T09:17:10.4       | 656.2       | 256                | (2029, 219, 59)    | (2107, 282, 93)         | PL    | –                       | –                    | –                    | –                           |
| 7  | 2009-01-29T11:19:27.4       | 265.6       | 139                | (127, 131, 84)     | (155, 143, 101)         | CutPL | $0.12^{+0.13}_{-0.14}$  | $28.1^{+0.7}_{-3.4}$ | $74.6^{+1.9}_{-9.1}$ | 0.82(0.74)                  |
| 8  | 2009-01-29T12:16:56.4       | 390.6       | 19                 | (44, 23, 15)       | (56, 28, 26)            | PL    | $1.49^{+0.08}_{-0.07}$  | $1.8^{+0.4}_{-0.4}$  | $7.1^{+1.4}_{-1.5}$  | 1.46(0.15)                  |
| 9  | 2009-01-29T12:17:36.5       | 54.7        | 11                 | (19, 11, 10)       | (34, 16, 32)            | PL    | $0.91^{+0.13}_{-0.13}$  | $15.0^{+1.9}_{-4.3}$ | $8.2^{+1.0}_{-2.3}$  | 0.28(0.95)                  |
| 10 | 2009-01-29T12:58:41.1       | 78.1        | 44                 | (–, 38, 29)        | (–, 47, 41)             | PL    | –                       | –                    | –                    | –                           |
| 11 | 2009-01-29T13:41:57.1       | 164.1       | 8                  | (21, 8, 11)        | (37, 10, 20)            | PL    | $1.45^{+0.14}_{-0.12}$  | $2.5^{+0.5}_{-0.6}$  | $4.1^{+0.8}_{-0.9}$  | 0.85(0.55)                  |
| 12 | 2009-01-29T13:43:27.9       | 210.9       | 7                  | (7, 9, 13)         | (13, 10, 26)            | CutPL | $-0.38^{+0.39}_{-0.55}$ | $4.0^{+0.8}_{-0.7}$  | $8.4^{+1.7}_{-1.4}$  | 0.53(0.78)                  |
| 13 | 2009-01-29T13:46:37.4       | 328.1       | 13                 | (97, 20, 19)       | (113, 27, 26)           | CutPL | $1.11^{+0.17}_{-0.18}$  | $4.3^{+0.2}_{-1.3}$  | $14.0^{+0.7}_{-4.3}$ | 0.87(0.56)                  |
| 14 | 2009-01-29T13:50:38.2       | 835.9       | 60                 | (156, 62, 82)      | (187, 67, 89)           | CutPL | $0.83^{+0.09}_{-0.09}$  | $5.5^{+0.3}_{-0.8}$  | $45.9^{+2.5}_{-6.4}$ | 1.10(0.34)                  |
| 15 | 2009-01-29T15:40:45.1       | 109.4       | 15                 | (35, 14, 14)       | (44, 16, 24)            | PL    | $1.48^{+0.09}_{-0.08}$  | $4.8^{+0.7}_{-0.9}$  | $5.3^{+0.7}_{-1.0}$  | 1.23(0.26)                  |
| 16 | 2009-01-29T16:51:40.5       | 265.6       | 90                 | (97, 85, 75)       | (148, 96, 98)           | CutPL | $0.28^{+0.12}_{-0.12}$  | $21.1^{+0.9}_{-2.9}$ | $56.1^{+2.4}_{-7.8}$ | 0.54(0.97)                  |
| 17 | 2009-01-29T16:59:58.8       | 109.4       | 6                  | (19, 6, 5)         | (24, 8, 19)             | PL    | $1.39^{+0.17}_{-0.15}$  | $2.6^{+0.7}_{-1.1}$  | $2.9^{+0.8}_{-1.2}$  | 0.78(0.60)                  |
| 18 | 2009-01-29T18:42:12.6       | 54.7        | 5                  | (17, 6, 7)         | (25, 8, 23)             | PL    | $1.38^{+0.19}_{-0.16}$  | $6.5^{+1.6}_{-1.7}$  | $3.6^{+0.9}_{-1.0}$  | 0.27(0.97)                  |

1: An event train of length  $N_{\text{bst}}$  is defined in §2.2.

2:  $N_{\text{T90}}$  and 1-sec rate around the burst are shown in a form of (XIS0, PIN, GSO). The former is a burst photon count during  $T_{90}$  defined in §3.1. The latter is extracted from 1-sec binned light curves in Figure 2.

3: Flux is shown in a unit of  $10^{-8}$  erg  $\text{s}^{-1}$   $\text{cm}^{-2}$ , and fluence is in  $10^{-9}$  erg  $\text{cm}^{-2}$  both in the 10–70 keV band.



**Table 2.** Spectral parameters of the three brightest short bursts.

| Spectral Model    | Parameter  | BST-7                                     | BST-14                                       | BST-16                                     |
|-------------------|--|---|--|--|
|                   | Time (2011-01-29)  | 11:19:27.4                                | 13:50:38.2                                   | 16:51:40.5                                 |
|                   | T90 (sec)  | 0.2656                                    | 0.8359                                       | 0.2656                                     |
|                   | Fluence <sup>1</sup> (10 <sup>-8</sup> erg cm <sup>-2</sup> )                    | 7.46 <sup>+0.48</sup> <sub>-0.82</sub>    | 4.60 <sup>+0.25</sup> <sub>-0.67</sub>       | 5.60 <sup>+0.24</sup> <sub>-0.72</sub>     |
| wabs <sup>2</sup> | $N_{\text{H}}$ (10 <sup>22</sup> cm <sup>-2</sup> )                              | (3.2 fix)                                 | (3.2 fix)                                    | (3.2 fix)                                  |
| CutPL             | Photon Index $\Gamma$  | 0.12 <sup>+0.13</sup> <sub>-0.14</sub>    | 0.83 ± 0.09                                  | 0.28 ± 0.12                                |
|                   | Cutoff Energy $E_{\text{cut}}$ (keV)   | 26.9 <sup>+4.4</sup> <sub>-3.8</sub>      | 65.7 <sup>+16.7</sup> <sub>-12.3</sub>       | 31.9 <sup>+4.8</sup> <sub>-4.1</sub>       |
|                   | PIN Flux <sup>3</sup> (10 <sup>-7</sup> erg s <sup>-1</sup> cm <sup>-2</sup> )   | 2.81 <sup>+0.18</sup> <sub>-0.31</sub>    | 0.55 <sup>+0.03</sup> <sub>-0.08</sub>       | 2.11 <sup>+0.09</sup> <sub>-0.27</sub>     |
|                   | Total Flux <sup>4</sup> (10 <sup>-7</sup> erg s <sup>-1</sup> cm <sup>-2</sup> ) | 4.01 <sup>+0.14</sup> <sub>-0.51</sub>    | 1.08 <sup>+0.07</sup> <sub>-0.18</sub>       | 3.21 <sup>+0.11</sup> <sub>-0.56</sub>     |
|                   | fit goodness $\chi^2_{\nu}$ ( $\nu$ )  | 0.82 (28)                                 | 1.10 (20)                                    | 0.54 (25)                                  |
|                   | figure   | fig.9(a1,2,5)                             | fig.9(b1,2,5)                                | fig.9(c1,2,5)                              |
| 2BB               | $kT_{\text{Low}}$ (keV)  | 5.28 <sup>+0.43</sup> <sub>-0.42</sub>    | 2.58 <sup>+0.47</sup> <sub>-0.34</sub>       | 3.97 ± 0.41                                |
|                   | $R_{\text{Low}}$ (km)  | 1.78 <sup>+0.20</sup> <sub>-0.18</sub>    | 2.88 <sup>+1.51</sup> <sub>-1.02</sub>       | 2.18 <sup>+0.31</sup> <sub>-0.27</sub>     |
|                   | $kT_{\text{High}}$ (keV)   | 20.5 ± 2.1                                | 20.9 <sup>+2.7</sup> <sub>-2.5</sub>         | 17.5 <sup>+1.8</sup> <sub>-1.7</sub>       |
|                   | $R_{\text{High}}$ (km)   | 0.142 <sup>+0.038</sup> <sub>-0.028</sub> | 0.0766 <sup>+0.0216</sup> <sub>-0.0165</sub> | 0.191 <sup>+0.047</sup> <sub>-0.0381</sub> |
|                   | PIN Flux <sup>5</sup> (10 <sup>-7</sup> erg s <sup>-1</sup> cm <sup>-2</sup> )   | 2.54 <sup>+0.12</sup> <sub>-0.35</sub>    | 0.45 <sup>+0.01</sup> <sub>-0.12</sub>       | 1.91 <sup>+0.12</sup> <sub>-0.29</sub>     |
|                   | Total Flux <sup>6</sup> (10 <sup>-7</sup> erg s <sup>-1</sup> cm <sup>-2</sup> ) | 4.05 <sup>+0.13</sup> <sub>-0.70</sub>    | 0.98 ± 0.02                                  | 3.05 <sup>+0.12</sup> <sub>-0.45</sub>     |
|                   | fit goodness $\chi^2_{\nu}$ ( $\nu$ )  | 0.62 (27)                                 | 0.79 (18)                                    | 0.58 (24)                                  |
|                   | figure   | fig.9(a3,5)                               | fig.9(b3,5)                                  | fig.9(c3,5)                                |
| 2BB + PL          | $kT_{\text{Low}}$ (keV)  | 5.85 <sup>+0.67</sup> <sub>-0.57</sub>    | 2.90 <sup>+0.30</sup> <sub>-0.28</sub>       | 4.35 <sup>+0.63</sup> <sub>-0.54</sub>     |
|                   | $R_{\text{Low}}$ (km)  | 1.45 <sup>+0.24</sup> <sub>-0.22</sub>    | 1.99 <sup>+0.37</sup> <sub>-0.33</sub>       | 0.565 <sup>+0.050</sup> <sub>-0.049</sub>  |
|                   | $kT_{\text{High}}$ (keV)   | 20.2 <sup>+2.5</sup> <sub>-2.3</sub>      | 20.9 <sup>+2.9</sup> <sub>-2.6</sub>         | 17.1 <sup>+1.9</sup> <sub>-1.8</sub>       |
|                   | $R_{\text{High}}$ (km)   | 0.139 <sup>+0.042</sup> <sub>-0.033</sub> | 0.0730 <sup>+0.0219</sup> <sub>-0.0167</sub> | 0.191 <sup>+0.052</sup> <sub>-0.041</sub>  |
|                   | $\Gamma_{\text{bst}}$  | 1.54 (fix)                                | 1.54 (fix)                                   | 1.54 (fix)                                 |
|                   | PL Flux <sup>7</sup> (10 <sup>-7</sup> erg s <sup>-1</sup> cm <sup>-2</sup> )    | 0.410 <sup>+0.190</sup> <sub>-0.195</sub> | 0.140 <sup>+0.092</sup> <sub>-0.093</sub>    | 0.339 <sup>+0.196</sup> <sub>-0.200</sub>  |
|                   | fit goodness $\chi^2_{\nu}$ ( $\nu$ )  | 0.48 (26)                                 | 0.68 (18)                                    | 0.49(23)                                   |
|                   | figure   | fig.14(a)                                 | fig.14(b)                                    | fig.14(c)                                  |

1: Fluences are estimated using the CutPL model in the 10–70 keV range with T90.

2: The interstellar absorption (wabs) is multiplied to each model.

3, 5, 7: Absorbed e X-ray fluxes in the 10–70 keV energy range at its average value.

4, 6, 8, 9: Absorbed X-ray fluxes in the 1–300 keV energy range at its average value.

**Table 3.** Spectral parameters of the accumulated weaker short burst. All the quoted errors are at the  $1\sigma$  level.

| Burst Emission                   |   |                                       |
|----------------------------------|---|---------------------------------------|
|                                  | Summed exposure (sec)   | 3.7                                   |
|                                  | Ave. fluence <sup>1</sup> (erg cm <sup>-2</sup> )                             | $6.61^{+0.04}_{-2.04} \times 10^{-9}$ |
| Spectral Model                   | Parameter   | Value                                 |
| PL ( $N_{\text{H}}$ fixed)       | $N_{\text{H}}$ (10 <sup>22</sup> cm <sup>-2</sup> )                           | 3.2 (fix)                             |
|                                  | Photon Index $\Gamma_{\text{bst}}$  | 1.5                                   |
|                                  | fit goodness $\chi^2_{\nu}$ ( $\nu$ )   | 2.05 (34)                             |
| PL                               | $N_{\text{H}}$ (10 <sup>22</sup> cm <sup>-2</sup> )                           | $5.4^{+0.8}_{-0.5}$                   |
|                                  | Photon Index $\Gamma_{\text{bst}}$  | $1.57 \pm 0.04$                       |
|                                  | Flux <sup>1</sup> (10 <sup>-8</sup> erg s <sup>-1</sup> cm <sup>-2</sup> )    | $1.7 \pm 0.1$                         |
|                                  | fit goodness $\chi^2_{\nu}$ ( $\nu$ )   | 1.29 (33)                             |
| CutoffPL                         | $N_{\text{H}}$ (10 <sup>22</sup> cm <sup>-2</sup> )                           | 3.2 (fix)                             |
|                                  | Photon Index $\Gamma_{\text{bst}}$  | $1.03 \pm 0.07$                       |
|                                  | Cutoff Energy $E_{\text{cut}}$ (keV)  | $62.9^{+14.5}_{-10.8}$                |
|                                  | Flux <sup>1</sup> (10 <sup>-8</sup> erg s <sup>-1</sup> cm <sup>-2</sup> )    | $2.3^{+0.1}_{-0.2}$                   |
|                                  | fit goodness $\chi^2_{\nu}$ ( $\nu$ )   | 0.81 (33)                             |
| 2BB                              | $N_{\text{H}}$ (10 <sup>22</sup> cm <sup>-2</sup> )                           | 3.2 (fix)                             |
|                                  | $kT_{\text{Low}}$ (keV)   | $1.68^{+0.17}_{-0.15}$                |
|                                  | $R_{\text{Low}}$ (km)   | $3.33^{+0.52}_{-0.46}$                |
|                                  | $kT_{\text{High}}$ (keV)  | $12.3^{+0.9}_{-0.8}$                  |
|                                  | $R_{\text{High}}$ (km)  | $0.140^{+0.021}_{-0.018}$             |
|                                  | Flux <sup>1</sup> (10 <sup>-8</sup> erg s <sup>-1</sup> cm <sup>-2</sup> )    | $2.5 \pm 0.2$                         |
|                                  | fit goodness $\chi^2_{\nu}$ ( $\nu$ )   | 1.63 (32)                             |
| 2BB + PL                         | $N_{\text{H}}$ (10 <sup>22</sup> cm <sup>-2</sup> )                           | 3.2 (fix)                             |
|                                  | $kT_{\text{Low}}$ (keV)   | $2.71^{+0.50}_{-0.48}$                |
|                                  | $R_{\text{Low}}$ (km)   | $1.16^{+0.41}_{-0.29}$                |
|                                  | $kT_{\text{High}}$ (keV)  | $13.3^{+2.0}_{-1.6}$                  |
|                                  | $R_{\text{High}}$ (km)  | $0.0905^{+0.0283}_{-0.0255}$          |
|                                  | $\Gamma_{\text{h}}$   | 1.53 (fix)                            |
|                                  | PL Flux <sup>1</sup> (10 <sup>-8</sup> erg s <sup>-1</sup> cm <sup>-2</sup> ) | $0.78 \pm 0.13$                       |
|                                  | fit goodness $\chi^2_{\nu}$ ( $\nu$ )   | 0.82 (31)                             |
| Persistent Emission <sup>2</sup> |   |                                       |
| BB + PL                          | $N_{\text{H}}$ (10 <sup>22</sup> cm <sup>-2</sup> )                           | $3.2 \pm 0.1$                         |
|                                  | $kT$ (keV)  | $0.65^{+0.02}_{-0.01}$                |
|                                  | $\Gamma_{\text{per}}$   | $1.54^{+0.03}_{-0.04}$                |
|                                  | Flux <sup>1</sup> (10 <sup>-10</sup> erg s <sup>-1</sup> cm <sup>-2</sup> )   | $1.40^{+0.05}_{-0.07}$                |
|                                  | fit goodness $\chi^2_{\nu}$ ( $\nu$ )   | 1.08 (278)                            |

1: Average fluence is evaluated in the 10–70 keV band assuming the 2BB+PL model. Flux are estimated in the 10–70 keV.

2: Values from Paper I. The quoted errors are converted to the  $1\sigma$  level.

## APPENDIX A: CORRECTION FOR THE P-SUM MODE XIS0

Here we describe further calibrations of the time assignments and responses of the P-sum (timing) mode XIS0, dedicated towards the present analyses.

$$R_{xy}(i) = \frac{1}{N-i} \sum_{j=0}^{N-1-j} x(j) \cdot y(i+j) \quad (i = 0, 1, \dots, N-1). \quad (\text{A1})$$

Figure A2(a) and (b) show cross-correlation coefficients of the 10–14 keV and 40–70 keV data, respectively. As clearly shown in these figures, no time lag was confirmed between the HXD 40–70 keV data (Figure A2b), while the cross-correlation peak of the 10–14 keV range appears at 31.25 ms in Figure A2(a). Thus, we assigned the time correction of 31.25 ms to the XIS0 data set ( $\text{TIME} - 0.0325$  s). This correction is consistent with the previous analyses of the persistent X-ray emission at §3.1 in Paper I. Individual light curves of XIS0 in Figure 5 were already corrected on this time lag of the 31.25 ms.

### A2 Response correction

For the XIS0 spectral analyses, we produced *rmf* and *arf* files based on the procedure stated in Matsuta et al. (2010). Since the P-sum spectral data is not widely utilized so far, it requires a careful calibration, we further included correction factors to *rmf* and *arf* files, as follows. The persistent X-ray emission from 1E 1547.0–5408 was already measured using the XIS1, XIS3, HXD-PIN, and HXD-GSO data in Paper I. We also produced the same persistent X-ray spectra from the XIS0, after eliminating bright short bursts, and compared it with that in Paper I. We fixed the spectral parameters at the values reported in Paper I, and only three parameters of the XIS0 response (a normalization factor, a slope and an offset of the gain) were left free to be fitted. Then, we determined the normalization factor, the slope and the gain to be 1.079, 0.90,  $-0.05$ , respectively. In this paper, we use these correction factors.

### A1 Timing correction

It is known that there is still a slight time lag ( $\sim 30$  ms) assigned to the P-sum mode of the XIS, even after including corrections related with read-out time delays, depending on the source position on the XIS CCD chip (see Matsuta et al. 2009). To study the burst light curves in detail, we further assigned an additional timing correction to the P-sum mode, comparing the HXD-PIN data, which was already accurately calibrated using the Crab pulsar (Terada et al. 2008). In order to evaluate the residual time lag, we compared the burst light curves of the XIS0 to that of HXD-PIN both in the 10–14 keV. We accumulated 5 short bursts in which the 10–14 keV photons were clearly detected in the HXD-PIN data. Panels in Figure A1 (left) are the 10–14 keV cumulative light curves of XIS0 and HXD-PIN, respectively, while panels in Figure A1 (right) are the 40–70 keV ones of HXD-PIN and HXD-GSO as a reference. As compared here, the 40–70 keV peaks correspond with each other, while a peak of the 10–14 keV XIS0 data comes slightly later than that of the HXD-PIN.

In order to quantitatively evaluate this XIS0 time lag, we calculated cross-correlations of them. The cross-correlation coefficient  $R_{xy}(i)$  for the  $i$ -th bin is calculated by

## APPENDIX B: THE STATISTICAL SIGNIFICANCES OF DETECTED BURSTS

We have already evaluated the detection significances in §2.2 using only the HXD-PIN data. Here we further evaluated the statistical significance of these detections combining the XIS, HXD-PIN, and HXD-GSO together. Especially, the XIS instruments are placed at different location in the *Suzaku* satellite, temporal coincidences of the X-ray events between the HXD and the XIS0 make the detection much plausible. A possibility to detect  $n$  events, from the Poisson distribution of its average  $\lambda$  count  $\text{sec}^{-1}$ , during a time duration of  $T$  can be written as  $P(\lambda, n) = (\lambda T)^n \exp(-\lambda T)/n!$ . Thus, multiplied by the independent instruments, the total probability of these bursts become  $P_{\text{total}} = P_{\text{XIS}} \cdot P_{\text{PIN}} \cdot P_{\text{GSO}}$ . Here we employ  $T = 1$  sec and corresponding burst rates listed in Table 1, together with average rate of  $\lambda_{\text{XIS0}} = 3.98$  counts  $\text{s}^{-1}$ ,  $\lambda_{\text{PIN}} = 0.76$  counts  $\text{s}^{-1}$ ,  $\lambda_{\text{GSO}} = 13.38$  counts  $\text{s}^{-1}$  (see §2.1). Considering the total bin number of  $n_{\text{bin}} = 4.5 \times 10^4$ , chance occurrence  $n_{\text{bin}} P_{\text{total}}$  of these bursts are estimated to be below  $10^{-5}$ . Therefore, we confirmed these events are indeed short bursts.

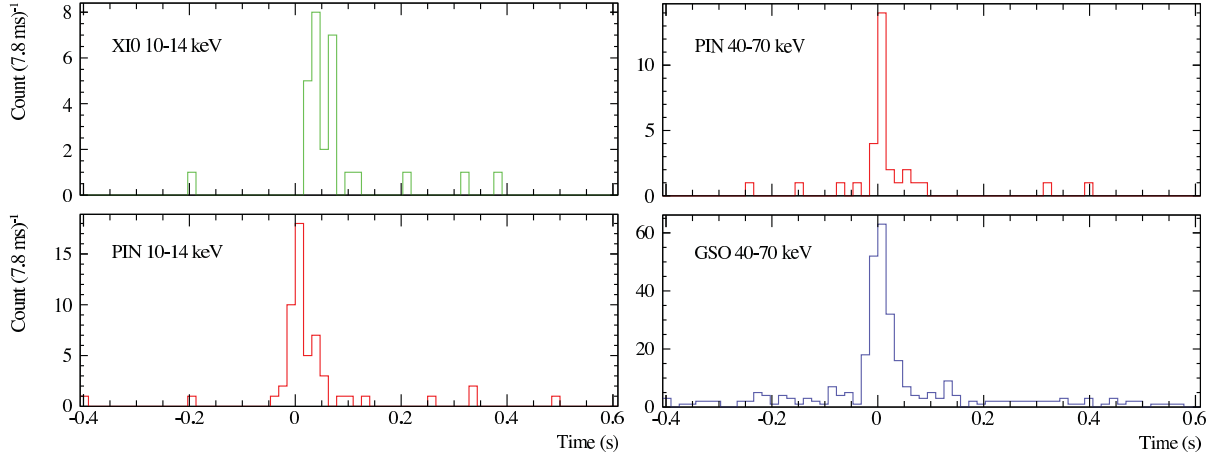


**Figure A1.** (left) Accumulated light curves of 5 short bursts (Burst-4,7, 9, 14, 16) from XI0 (top) and for HXD-PIN (bottom) both in the 10–14 keV energy range. (right) Same as the left panels, but from the HXD-PIN (top) and HXD-GSO (bottom) both in the 40–70 keV energy range. Burst-2, 6, 7, 9, 10, 11, 14, 16 and 18 are used for the accumulation.

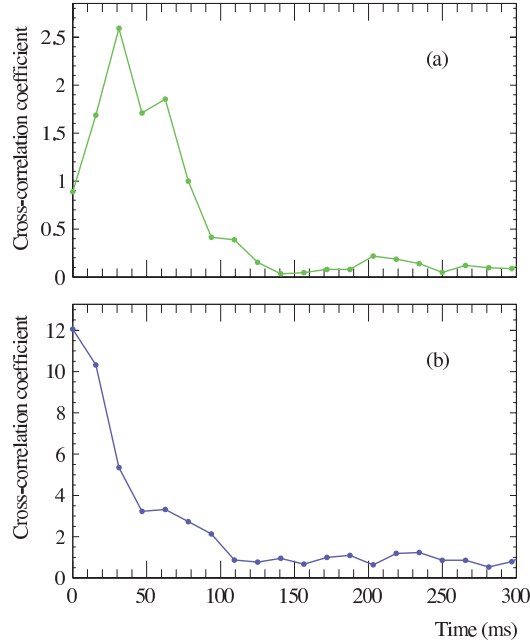


**Figure A2.** Cross-correlation coefficients calculated through equation (A1). Panel (a) is obtained from the P-sum mode XI0 data to the HXD-PIN data both in the 10–14 keV energy range, corresponding to the data in figure A1(left). Panel (b) is obtained from the HXD-GSO data to the HXD-PIN data both in the 40–70 keV energy range, corresponding to those in figure A1(right).

### APPENDIX C: CHECK OF THE DATA LOSS

The burst data (except for Burst-6 and Burst-10), were examined for possible losses or pile-ups, through the same procedure as applied to the much brighter burst from SGR 0501+4516 recorded with *Suzaku* in 2008 (Enoto et al. 2009). There are three possible forms of the data loss; (1) dead time in the event handling at the analog electronics (HXD-AE), (2) the limited event transfer rate from HXD-AE to the digital electronics (HXD-DE), and (3) that from HXD-DE to the spacecraft data processor. Since the peak

count rates of these bursts are less than  $\sim 60$  counts  $(15.6 \text{ ms})^{-1}$ , the effect of (1) is estimated to be at most  $\lesssim 8\%$ , and on average  $\sim 1\%$ , since the data acquisition time ( $20 \mu\text{s}$ ) is much shorter than the burst event interval. Pileup is much less effective due to a short time window for the pulse height latch. These event data were not lost in the above (2) and (3) processes as well, since the event rates were much smaller than the maximum limits; 4 kHz for (2) and 400 counts  $(4 \text{ sec})^{-1}$  for (3). Thus, our samples are free from the data loss due to the dead-time or the event pile-ups. Since the dead-

time effect is typically  $\sim 1\%$  for most cases, we does not correct the dead-time.